Integrated Thermo-Hydro-Mechanical Workflow for Modeling CO_2 Storage with Fault Activation Risk

Zijun Wei[1,2], Ke Gao[2*], and Sanbai Li[3*]

[1]School of Environment, Harbin Institute of Technology
[2]Department of Earth and Space Science, Southern University of Science and Technology, Shenzhen
[3]School of Resources and Safety Engineering, Central South University, Changsha

Summary

Carbon capture and storage is crucial in combating global climate change by effectively mitigating carbon emissions. Deep saline aquifers possess the largest identified storage capacity, making them the preferred storage location. However, when CO_2 is injected underground, it tends to escape through interconnected fractures or reactivated faults toward the ground due to buoyancy. Thus, studying the impact of CO_2 injection on faults and the feedback effect of fault activation on CO_2 leakage is significant. In this work, we develop and validate a fully coupled thermo-hydro-mechanical (THM) model to simulate mutual interactions between CO_2 injection, fault movement, and CO_2 plume propagation. We further analyze the elastoplastic failure behavior of faults, and our simulation results show that fault activation leads to a dramatic change in permeability properties, which are highly heterogeneous and exhibit a strong dependence on plastic damage. In addition, the hydraulic behaviors of reservoirs are compared under closed (no-flow) and more generally open (hydrostatic pressure) boundaries. In a decades-long industrial-scale CO_2 continuous injection scenario, the reservoir pressure disturbance under closed boundaries reaches 39%, whereas the pressure disturbance under open boundaries is less than 1%. This stark contrast underscores the paramount importance of boundary conditions and highlights the necessity to delve into whether effective fluid trapping zones can be formed in the vicinity of faults. Finally, we focus on optimizing decoupling strategies for tackling this multiphase, large-scale, and nonlinear THM problem. We compare six decoupling sequences exhaustively, and the test results reveal that the sequence in which the fields are solved significantly impacts the stability and convergence rate of the numerical model. Specifically, the sequence of first seepage, then temperature, and finally displacement fields yields the best stability and convergence and also maintains precision, offering a valuable reference for tackling such THM challenges efficiently.

Introduction

As accepted by most scientists, the increase in average global temperature over the past 50 years is likely due to the rise in anthropogenic greenhouse gases in the atmosphere, such as methane and CO_2 (Metz et al. 2005). Underground storage of CO_2 is considered an effective means to combat global warming. Injecting CO_2 into "depleted oil and gas reservoirs, deep saline aquifers, and coal seams has been suggested as an important method" for mitigating greenhouse gas emissions (Rutqvist et al. 2002). Among these, the caprocks are frequently traversed by numerous wells for depleted oil and gas reservoirs, potentially compromising the integrity of storage confinement. For coal seams, due to the strong adsorption of CO_2 by coal, CO_2 storage in economically nonviable coal beds has been suggested and operated in some pilot projects globally (White et al. 2005; Bachu 2007). However, the ultralow permeability of coal seams hinders the success of coal seams in storing CO_2, leading to this method being largely abandoned in practical applications (Celia et al. 2015). According to Metz et al. (2005), deep saline aquifers exhibit the greatest recognized storage capacity and are far more prevalent worldwide compared with hydrocarbon reservoirs, which makes them the preferred storage location for large-scale carbon capture and storage (CCS) activities.

In principle, sedimentary basins, which feature layered sequences of permeable rocks like sandstones or carbonates, topped by impermeable caprocks like shales, are viable options for CO_2 sequestration, provided that they remain unfaulted. Based on this consideration, we should try to avoid large faults and crack development areas when selecting CO_2 storage sites to reduce the CO_2 leakage risk. However, the strata are often naturally fractured and even accompanied by large faults. For instance, "natural CO_2 flow through active fault zones was observed during the 1997 Umbria-Marche seismic sequence in northern Italy" (Cappa and Rutqvist 2011), and Miller et al. (2004) proposed that "aftershocks of large earthquakes may be driven by the coseismic release of trapped, high-pressure fluids (CO_2) propagating through damaged zones created by the mainshock." Besides this, the geomechanical response of faults during CO_2 injection has also been observed at the In Salah CO_2 storage site, where the "flow associated with the injection of CO_2 does extend several kilometers laterally within the reservoir, following the fault zone" (Ringrose et al. 2009; Vasco et al. 2010).

Additionally, significant density contrast exists between injected CO_2 and saline water. The density of CO_2 is about 250–800 kg/m³ at a depth range of 600–1000 m, depending on temperature and pressure gradients (Bachu 2003), while the density of saline water may exceed 1200 kg/m³ (Celia et al. 2015). Thus, when CO_2 is injected underground, it tends to escape toward the ground through interconnected fractures or reactivated faults due to strong buoyancy; CO_2 sequestration is expected to form plumes that cover a significant area extent (Pruess 2008). Meanwhile, some studies have shown that for industrial-scale CO_2 storage projects, the injection of CO_2 can cause fluid pressurization that impacts a region spanning beyond a 100-km radius (Pruess 2004; Birkholzer and Zhou 2009). Within such a wide range, it is difficult to completely avoid weak areas with major faults or large cracks. Therefore, studying how CO_2 injection affects fault behaviors and the feedback effects brought by fault activation has practical significance in assessing the security of CCS activities.

CO_2 sequestration coupled with fault activation is a comprehensive multiphase and multiphysics problem. To capture the migration pattern of CO_2 plumes, it is necessary to calculate the multiphase seepage field. Mechanical deformation and stress fields also need to be included to determine whether faults will become active. In addition, the strong dependence of CO_2 density on temperature, combined

*Corresponding author; email: lisb6@csu.edu.cn; gaok@sustech.edu.cn

Original SPE manuscript received for review 1 October 2024. Revised manuscript received for review 27 January 2025. Paper (SPE 225428) peer approved 7 February 2025.

with the temperature differences between the injected CO_2 and the host formation, can have a substantial influence in many situations (Gasda et al. 2013). For instance, CO_2 can migrate upward along the activated faults or high-permeability fractures to shallower pressure environments, posing the potential for swift depressurization and resulting in a phase change to the gas phase, which enhances Joule-Thomson cooling (Pruess 2005Pruess 2008; Celia et al. 2015), and then the thermal stress may have a potential impact on fault slip and seismic activities (Ganguli et al. 2018; Ganguli and Sen 2020; Meguerdijian et al. 2022; Sáez-Leiva et al. 2023; Wu et al. 2023). Therefore, the CO_2 storage problem considering fault activation entails a THM modeling. Rutqvist et al. (2002) conducted a pioneer work in analyzing the CO_2 storage problem with a THM model, using a sequential coupling method to link two widely validated commercial software (i.e., TOUGH2 and FLAC). They used TOUGH2 + FLAC to investigate fault instability and crustal deformation (Rutqvist et al. 2007; Cappa et al. 2009). Subsequently, Cappa and Rutqvist (2011) developed a hydromechanical (HM) coupling model for fault reactivation investigation due to CO_2 injection in deep aquifers. They compared three modeling approaches for analyzing fault instability processes, finding that the HM behavior of faults can be appropriately represented with a finite-thickness element and isotropic plasticity approach. However, they neglected the temperature variation in the rock mass and fluid, leading to an assessment conclusion based on the isothermal assumption.

Recent investigations provide insights into fault activation. Rutqvist et al. (2016) summarized the insights gained from modeling investigations focusing on fault reactivation, induced seismicity, and the possibility of CO_2 escape caused by CCS activities. They suggested that heterogeneous fault properties could effectively reduce the likelihood of inducing seismicity. Additionally, they argued that brittle rocks should be avoided when selecting CO_2 storage sites, as "they are more prone to injection-induced seismicity and permanent damage." March et al. (2018) assessed the CO_2 storage potential in naturally fractured reservoirs, which have received little attention due to the risk of CO_2 leakage along high conductivity fractures. Their results show that "naturally fractured reservoirs can be used to store CO_2"; however, their study overlooked the influence of fluid injection on the stress field and the disturbance effect of mechanical stress on fracture width. Fu et al. (2017, 2021) developed an interest in fracture propagation caused by CO_2 injection. They established a coupled THM fracturing model (i.e., GEOS) to simulate the initiation and growth of fractures. In these works, they summarized that the generation of cracks could improve the storage efficiency of CO_2 under carefully designed stimulation treatments. They believed that a precise pressure control can ensure the opening of cracks without penetrating the caprock and improve injection efficiency. However, they also pointed out that "sustaining such a fracture may lead to continuously increasing pressure until the caprock fractures," which poses additional challenges to the injection process.

Meguerdijian and Jha (2021) quantified "the fault leakage dynamics" based on the leakage magnitude and dip angle. They emphasized that a smaller induced slip event could potentially result in a greater leakage magnitude than a larger one, indicating that the risks of induced seismicity and leakage should not be considered synonymous. Luu et al. (2022) developed a coupled HM model to simulate induced seismicities from CO_2 injection in the Illinois Basin; the modeling indicates that, in addition to changes in fluid pressure, considering changes in poroelastic stress is important for accurately simulating seismicity rate. Glubokovskikh et al. (2022) conducted a case study on Stage 2C of the "CO2CRC Otway Project" (Victoria, Australia), where "a small leakage-like injection triggered seismicity below the felt levels." Their site monitoring and simulation results indicated that "the reactivation occurred when CO_2 plume reached the fault," and they pointed out that the activation of the pre-existing fault may not be caused by pressure buildup, but rather by the injection of CO_2 gas that "weakens the rocks filling the fault gouge, thus making the fault more prone to reactivation."

Due to the complexity of multiphase, multicomponent problems, a common approach involves utilizing distinct specialized simulators, such as TOUCH2 + FLAC or MUFITS + FLAC (Kanin et al. 2024). Users need to write their interfaces to call different software functions and transfer data. In contrast, in this paper, we develop a fully coupled and integrated multiphase THM model, where all governing equation sets are formulated within COMSOL Multiphysics®. Moreover, given that fully coupled computing is overly time-consuming, we have compared multiple decoupling schemes and aimed to find a relatively robust and efficient decoupling strategy for addressing these large-scale, nonlinear multiphase THM challenges. In addition, concerning the numerical study on fault activation induced by CO_2 injection, we note that there is limited discussion on diverse boundary conditions. Researchers frequently employ tailored boundary conditions to enhance fault activation, such as 2D axisymmetric models (Cappa and Rutqvist 2011; Rinaldi et al. 2015; Meguerdijian and Jha 2021), akin to a conservative risk assessment that assumes the worst-case scenario. Specifically, Rinaldi et al. (2015) simplified the geometric configuration to be symmetrical and imposed no-flow boundaries for a high reservoir pressure. Given the inherent randomness of geological structures, it is evident that such symmetric or impermeable boundary conditions represent merely specific cases (Hansen et al. 2013). Hence, we posit that it is imperative to delve into more generalized scenarios. To this end, we have compared the effects of more general open boundaries with those of impermeable boundaries on fault activation status, elucidating the role of boundary conditions in shaping numerical simulation outcomes.

This paper is organized as follows. In the "Methods" section, we introduce the governing systems, constitutive models of the fault, and the implementation of the coupled multiphase THM model. In the "Numerical Verification" section, we assess the reliability of our numerical model by comparing it against two analytical models. In the "Application in 3D Fault Activation Model" section, we conduct numerical studies on fault activation based on 3D structures of the fault system. In the "Discussion" section, we conduct an in-depth discussion on the influence of decoupling order on the stability of numerical systems. Finally, in the "Conclusions" section, we summarize the main results and findings of this work.

Methods

Mass Balance Laws. Introducing pure CO_2 into an underground saline aquifer results in the formation of a two-phase system (i.e., the CO_2-rich and brine phases). In fact, CO_2 is slightly miscible with the brine, and CO_2 solubility is approximately 5% by mass under general reservoir conditions (Nordbotten et al. 2005). A smaller volume fraction of H_2O, less than 1% by volume (Celia et al. 2015), can evaporate into the CO_2-rich phase. Consequently, we are dealing with a multiphase, multicomponent complex system when injecting CO_2 into a saline aquifer. Here, the evaporation of brine is ignored. Similarly, given that CO_2 dissolution exerts negligible influence on both the pore pressure field and faults' stress state (Meguerdijian et al. 2022), its weak solubility is also overlooked. Thus, the governing equation can be simply expressed as (Celia et al. 2015)

$$\frac{\partial\left(\rho_i s_i \phi\right)}{\partial t} + \nabla \cdot \left(\rho_i \mathbf{u}_i\right) = Q_i \qquad i = 1, 2\,, \tag{1}$$

where ρ_i is the density of phase i ($i = 1$ and $i = 2$ for CO_2 and brine, respectively); s_i is the saturation (volume of phase per volume of pores) of phase i; ϕ is the porosity; and Q_i represents sources or sinks of mass in phase i. The volumetric fluxes are determined using the extended Darcy's law:

$$\mathbf{u}_i = -\frac{k_{ri}}{\mu_i}\mathbf{K}\cdot(\nabla p_i - \rho_i \mathbf{g}), \tag{2}$$

where $\mathbf{K}$ is the absolute permeability tensor of porous media; k_{ri} represents the relative permeability of fluid phase i; μ_i represents the dynamic viscosity of phase i; p_i denotes fluid pressure of phase i; $\mathbf{g} = (0, 0, -g_{\text{const}})$ denotes the gravity acceleration vector; and g_{const} is the value of local gravity acceleration.

To solve Eq. 1, a set of auxiliary equations needs to be added, i.e.,

$$s_1 + s_2 = 1, \tag{3}$$

and

$$p_c = p_n - p_w, \tag{4}$$

where p_c represents the capillary pressure, which is the difference between the two-phase pressures, and p_n and p_w represent the fluid pressures of the nonwetting and wetting phases, respectively. The nonwetting phase pressure always exceeds the wetting phase pressure to ensure that the capillary pressure is positive. For the CO_2-brine system, the CO_2-rich phase is the nonwetting phase.

There are two common analytical models for determining capillary pressures and relative permeability; these are the Brooks and Corey (1966) model and van Genuchten (1980) model, which define the functional relationship between capillary pressure and saturation. In this paper, we adopt the van Genuchten (v-G) model:

$$\begin{aligned} &\overline{s_i} = (s_i - s_{ri})/\left(1 - \sum_{j=1}^{N} s_{rj}\right),\ p_c = p_{ec}\left((\overline{s_w})^{-1/m_{vG}} - 1\right)^{1-m_{vG}} \\ &k_{r_{s_w}} = (\overline{s_w})^{l_{vG}}\left(1 - \left(1 - (\overline{s_w})^{1/m_{vG}}\right)^{m_{vG}}\right)^2,\ k_{r_{s_n}} = (\overline{s_n})^{l_{vG}}\left(1 - \left(1 - \overline{s_n}\right)^{1/m_{vG}}\right)^{2m_{vG}} \end{aligned}, \tag{5}$$

where $\overline{s_i}$ is the effective saturation of each phase; s_{ri} denotes the residual saturation of each phase; p_{ec} is the entry capillary pressure; $k_{r_{s_w}}$ and $k_{r_{s_n}}$ represent the relative permeability of the wetting and nonwetting phases, respectively; and m_{vG} and l_{vG} are constitutive constants.

In this paper, the effects of structural distortions and variations in temperature on the pore pressure distribution have been considered based on the thermoporoelastic theory. The volume source term in Eq. 1 has the following form (Coussy 2003; Li et al. 2016):

$$Q_i = -\rho_i b\frac{\partial \varepsilon_{\text{vol}}}{\partial t} + 3\rho_i \alpha_m \frac{\partial T}{\partial t} + q_i, \tag{6}$$

where b is the Biot coefficient; ε_{vol} is the volumetric strain of structure; T denotes the temperature; $\alpha_m = \phi\sum \alpha_{fi}s_i + (1-\phi)\alpha_s$ is the line thermal expansion coefficient of rock mass; α_s and α_f denote the thermal expansion coefficient of solid and fluid phases, respectively; and q_i signifies external sources or sinks (e.g., injection or production wells).

Momentum Balance Laws. Assuming quasistatic conditions (neglecting the acceleration component), the equations governing momentum balance within the deformable media can be formulated as follows:

$$\nabla\cdot\boldsymbol{\sigma} + \rho_m \mathbf{g} = \mathbf{0}, \tag{7}$$

where σ is the total stress tensor and $\rho_m = \phi\sum \rho_{fi}s_i + \left(1-\phi\right)\rho_s$ denotes the saturated rock mass density. The principle of effective stress elucidates that the total stress borne by a rock mass is shared collectively by the rock skeleton and the pore fluid, where the Biot coefficient quantifies the proportion of total stress attributed to the fluid. Consequently, the total stress can be expressed in the following form:

$$\boldsymbol{\sigma} = \mathbf{C}:(\boldsymbol{\varepsilon} - \boldsymbol{\varepsilon}_{th} - \boldsymbol{\varepsilon}_{pl}) - bp\mathbf{I}, \tag{8}$$

where $\mathbf{C}$ represents the stiffness matrix; $\boldsymbol{\varepsilon}$ represents the total strain, assuming infinitesimal deformation, in the form of $\boldsymbol{\varepsilon} = \frac{1}{2}\left(\nabla\mathbf{s} + (\nabla\mathbf{s})^{\mathrm{T}}\right)$; $\mathbf{s}$ denotes the displacement vector; $\boldsymbol{\varepsilon}_{th} = \alpha_m(T - T_0)\mathbf{I}$ denotes the thermal strain tensor; T denotes the current temperature, whereas T_0 signifies the initial temperature; $\mathbf{I}$ stands for the identity matrix; $\boldsymbol{\varepsilon}_{pl}$ denotes the plastic strain; and $p = \sum p_i s_i$ is the total average pore pressure.

Energy Balance Laws. Based on the local thermal equilibrium theory, the temperatures of the solid phase and all fluid phases are assumed to be equal, and only one energy conservation equation is needed to describe the system's thermodynamic behavior. The energy conservation equation then has the following form, reformulated as temperature T (Lewis and Schrefler 1998; Nield and Bejan 2017):

$$(\rho C_p)_{\text{eff}}\frac{\partial T}{\partial t} + \sum_i \left(\rho_{fi}C_{p,fi}\mathbf{u}_i\cdot\nabla T\right) + \nabla\cdot\left(-k_{\text{eff}}\nabla T\right) = Q, \tag{9}$$

where $(\rho C_p)_{\text{eff}} = \phi\sum \rho_{fi}C_{p,fi}s_i + \left(1-\phi\right)\rho_s C_{p,s}$ denotes the equivalent volumetric heat capacity of rock mass; $C_{p,s}$ and $C_{p,fi}$ represent the isobaric heat capacity of solid and fluid phases, respectively; $\mathbf{u}_i$ is the Darcy velocity of fluid phase i; $k_{\text{eff}} = \phi\sum k_{fi}s_i + \left(1-\phi\right)k_s$ is the effective thermal conductivity of rock mass; k_s and k_{fi} represent the thermal conductivity of solid and fluid phases, respectively; and Q denotes the external heat source or sink.

The thermophysical properties of CO_2 are sensitive to temperature and pressure, and the three-phase point of CO_2 (T = 31.1°C, P = 7.37 MPa) can be readily reached under the reservoir environment, leading to the possibility of CO_2 undergoing phase transition during transportation. Therefore, an accurate equation of state is needed for the coupled THM model. In this paper, the density of CO_2 is determined by the Span-Wagner model (Span and Wagner 1996), which has been recognized as the benchmark model for evaluating CO_2 density. The Span-Wagner model directly provides information on the density and isobaric pressure heat capacity of CO_2. The partial derivative properties—compression coefficient $\chi_f = \left(1/\rho\right)\left(\partial\rho/\partial p\right)$ and volumetric thermal expansion coefficient $\alpha = \left(-1/\rho\right)\left(\partial\rho/\partial T\right)$—are

numerically evaluated according to their definitions. Additionally, the transport properties of CO_2 (i.e., dynamic viscosity and thermal conductivity are determined by the residual theory models (Huber et al. 2016; Laesecke and Muzny 2017).

The National Institute of Standards and Technology has published a "REFPROP" data set, accessible at "https://webbook.nist.gov/cgi/fluid.cgi?ID=C124389&Action=Page," which contains the latest and most accurate thermophysical data for CO_2. The thermophysical properties of CO_2 calculated based on the aforementioned benchmark models can be retrieved from this data set. To ascertain the thermophysical properties of CO_2, we import the REFPROP data set into COMSOL Multiphysics® and generate interpolated functions for its properties based on temperature and pressure, spanning a wide range of temperatures from 270 K to 500 K and pressures from 0.1 MPa to 100 MPa.

Constitutive Model of the Fault. In this work, we conduct a comprehensive elastoplastic failure analysis for the fault. For the sake of numerical stability, we adopt the Drucker-Prager yield criterion as an indicator for the occurrence of fault slip and nonreversible deformations. The Drucker-Prager yield criterion, similar to the Mohr-Coulomb criterion but numerically more stable (Nguyen et al. 2019), utilizes a smooth approximation of the Mohr-Coulomb yield surface for continuum modeling of yielding in 3D scenarios (Zhao and Jha 2021). It is worth noting that the Drucker-Prager criterion is exclusively applied to the fault zones, whereas other regions' rock masses are treated as isotropic and elastic. In this study, we have adopted an inscribed version of the Drucker-Prager criterion with the associated flow rule, and the corresponding yield function is as follows (Zhao and Jha 2021):

$$F = \sqrt{J_2} + \alpha I_1 - \omega, \tag{10}$$

$$\alpha = \frac{2\sin\theta}{\sqrt{3}(3-\sin\theta)}, \qquad \omega = \frac{2\sqrt{3}c\ \cos\theta}{3-\sin\theta}, \tag{11}$$

where J_2 represents the second invariant of the deviatoric stress tensor; I_1 denotes the first principal invariant of the stress tensor; and α and ω are related to the internal friction angle (θ) and cohesion (c). When $F = 0$, the material begins to experience plastic failure, the corresponding area of the fault is considered to be activated, and the increment of plastic strain can be calculated by $d\varepsilon_{pl} = d\lambda \left(\partial F/\partial\sigma\right)$.

In addition to the criteria for determining fault activation, there are also various constitutive models for the permeability of faults. The geometric modeling of faults can be roughly divided into two types according to researchers' handling of the fault zone. One type ignores the thickness of the fault, utilizing the cubic law to describe the permeability of the fault (Guglielmi et al. 2015; Cappa et al. 2018; Rutqvist et al. 2020). However, this approach makes it impossible to characterize the heterogeneity between the damaged area and the fault core (Shipton and Cowie 2003). The above two regions exhibit distinct HM properties (Faulkner et al. 2006; Guglielmi et al. 2008; Cappa 2009), causing the entire fault zone to act either as a barrier or as a high conductivity channel (Caine et al. 1996). Another type of fault permeability model considers the thickness of the fault for modeling and meshing. We note that these models can be related to porosity and volumetric strain (Rutqvist et al. 2002; Cappa and Rutqvist 2011; Kanin et al. 2024). In this paper, we adopt the latter. The advantage of this approach lies in its ability to naturally establish a consistent permeability connection across both the elastic and plastic deformation stages.

Overall, the permeability evolution pattern caused by fault activation is complex. On-site fault reactivation experiments and monitoring results indicate significant differences in permeability before and after fault reactivation. Zappone et al. (2021) conducted an injection experiment at Mont Terri, and the results showed that estimated transmissivity increased by one order of magnitude with fault reactivation. Guglielmi et al. (2021) conducted field experiments on the tens-of-meter scale and found that "significant fluid leakage occurs along the initially low-permeability shale faults when faults are activated." Their monitoring results displayed a sudden threshold phenomenon (i.e., the fault permeability underwent a sharp increase by two to five orders of magnitude after activation). Moreover, they pointed out that the expansion slips on the fault plane are unable to explain the observed leakage behavior. As the simple model based on volumetric strain cannot capture the step change in permeability caused by fault activation, we combine the work of Guglielmi et al. (2015), and a fixed enhancing factor is applied when rupture occurs. On this basis, we make minor modifications to the Chin et al. (1998) model. Subsequently, we use the following permeability model to characterize the activation behavior of faults:

$$\begin{aligned} &\phi = 1 - (1-\phi_0)\mathrm{e}^{-\varepsilon_{\mathrm{vol}}}, \\ &k = k_0\left(\frac{\phi}{\phi_0}\right)^n \quad \text{before activation}, \\ &k = E_n \times k_0\left(\frac{\phi}{\phi_0}\right)^n \quad \text{after activation}, \end{aligned} \tag{12}$$

where ϕ_0 is the initial porosity; k_0 is the initial permeability; ϕ and k represent the current porosity and permeability, respectively; $\varepsilon_{\mathrm{vol}}$ represents the volumetric strain (including volumetric elastic strain and volumetric plastic strain); and E_n is the enhancing factor on fault permeability. Because the deformation of rock masses is usually small, we adopt another form for the relationship between porosity and volumetric strain, $\phi = 1 - (1-\phi_0)e^{-A\times\varepsilon_{\mathrm{vol}}}$, as proposed by Kanin et al. (2024), where A is an amplification factor to highlight the impact of structural deformation on the permeability field. Furthermore, we assume that the weak structures (like natural fractures) within the fault zone are randomly distributed so that the permeability tensor can be treated as isotropic.

Implementation Approach. For simulating CO_2 storage in deep saline aquifers, the aforementioned governing equations (Eqs. 1 through 12) have all been formulated and constructed within the COMSOL Multiphysics® platform. The software serves as a versatile numerical tool designed to solve partial differential equations. Individuals have the capability to formulate their custom partial differential equations and define their own constitutive relationships, such as different fault failure criteria and specialized fault permeability models. All equations are based on the finite element method for spatial discretization, thus avoiding the tedious process of transforming mesh and data information due to different discretization methods. Due to the integration of the governing equations within a unified platform, COMSOL supports the simultaneous solution of these equations to enable fully coupled simulations. Simultaneously, it also accommodates decoupling approaches, permitting flexible adjustment of the equation solution sequence to achieve diverse decoupling strategies. We compare various decoupling sequences, and one of the most robust solutions is shown in the flow chart in **Fig. 1**. Specifically, considering the contribution of the fluid flow to the energy equation in the form of thermal convection, we first calculate the seepage field. After calculating the seepage field, relevant variables such as fluid pressure, saturation, and velocity are updated to calculate the temperature field. The updated temperature and pore pressure information is then provided to calculate the thermal expansion and effective stress.

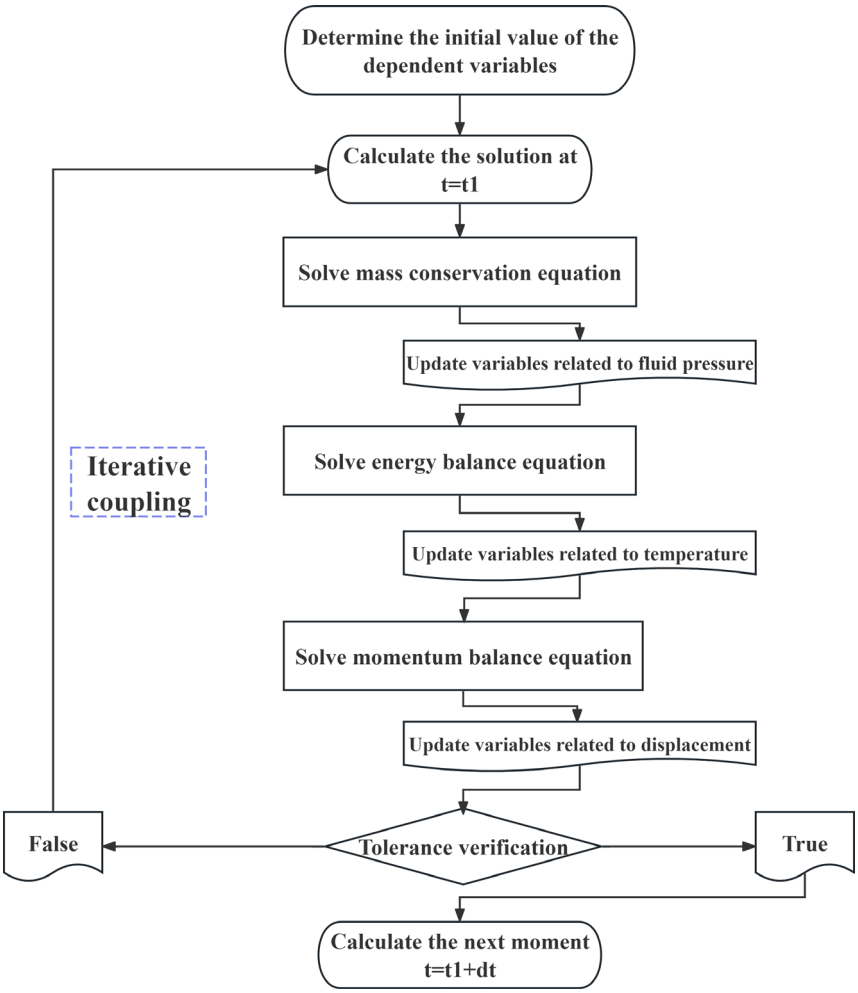

Fig. 1—Flow chart of a robust decoupling sequence.

After solving the momentum balance equation, the porosity and permeability are updated, and the next iteration is carried out to solve the seepage field again. To tackle the above equation system, we adopt the Newton method while utilizing a fully implicit backward difference format for time discretization. Convergence of the iteration is deemed achieved when the difference in dependent variables between consecutive iteration steps diminishes below a specified tolerance level. Subsequently, we proceed to solve the next time interval, employing a tolerance threshold of 1×10^{-4}. Our solver incorporates an adaptive timestepping method, which includes a predefined maximum iteration cap of 10 and a constraint on the maximum timestep size of 0.1 year (a).

Numerical Verification

The primary objective of this section is to verify the numerical model developed in this paper against two analytical models, demonstrating the robustness and precision of our numerical approach. Specifically, we aim to contrast our model against the Terzaghi consolidation model (Ferronato et al. 2010), serving as a benchmark for the HM coupling component, and the 1D nonisothermal thermal consolidation model (Bai 2005), validating the THM coupling aspect. Additionally, the isolated two-phase flow component of the numerical model has been validated through comparison with the Buckley-Leverett analytical model, referring to the example provided by COMSOL Multiphysics® v. 6.0 (2024).

Terzaghi Consolidation Model. The model domain is presented in **Fig. 2a**. The Terzaghi consolidation model targets saturated soil as its research subject, delineating the process of pore pressure gradually diminishing and the soil undergoing compaction under stress loading. The boundary conditions of the model are as follows: Regarding the displacement field, the lateral and bottom boundaries are configured as roller boundaries, preventing normal displacement, while the top boundary is subject to a stress condition; regarding the seepage field, the lateral and bottom boundaries exhibit impermeability, while the top boundary functions as a free-drainage boundary with no pressure head. The initial conditions and analytical solution are given by Ferronato et al. (2010):

$$\begin{aligned} p(z,t=0) &= \frac{bM}{K_u+4/3G}p_L, \\ u(z,t=0) &= \frac{1}{K_u+4/3G}p_L(L-z), \end{aligned} \tag{13}$$

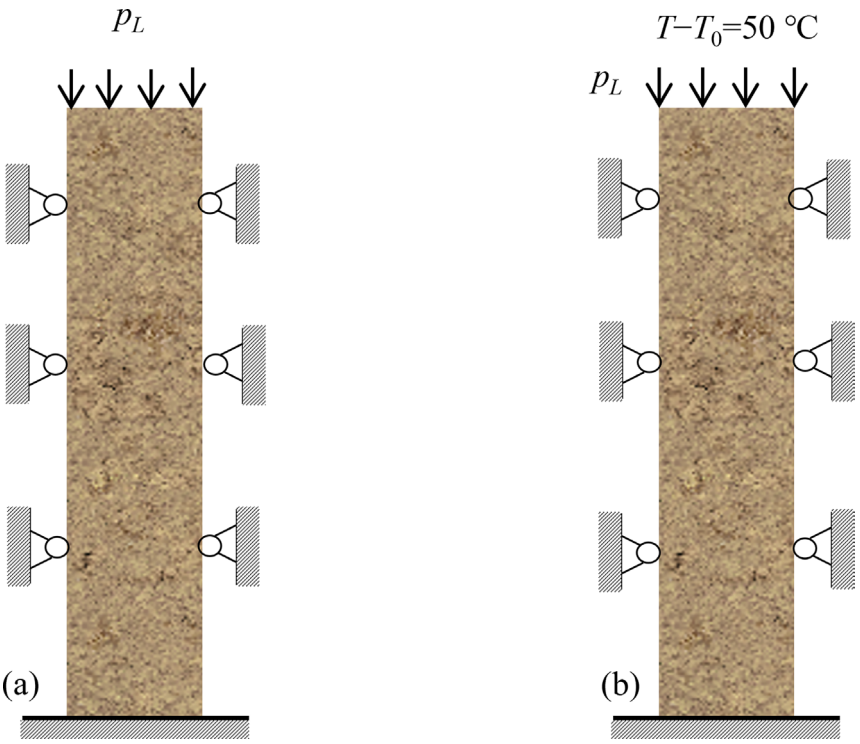

Fig. 2—Schematic description of the model domain and its boundary conditions: (a) Terzaghi consolidation model and (b) nonisothermal consolidation model.

$$p(z,t) = \frac{4}{\pi} p_0 \sum_{m=0}^{\infty} \left(\frac{1}{2m+1} \exp\left[\frac{-(2m+1)^2 \pi^2 ct}{4L^2} \right] \sin\left[\frac{(2m+1)\pi z}{2L} \right] \right),$$
$$u(z,t) = u_0 + C_m p_0 \left\{ (L-z) - \frac{8L}{\pi^2} \sum_{m=0}^{\infty} \frac{1}{(2m+1)^2} \exp\left[\frac{-(2m+1)^2 \pi^2 ct}{4L^2} \right] \cos\left[\frac{(2m+1)\pi z}{2L} \right] \right\}, \quad (14)$$

where b is the Biot coefficient; $M = 1/\left[\phi c_f + (b-\phi) c_s\right]$ is the Biot modulus; and c_s and c_f are the compressibility of solid and fluid, respectively. Other auxiliary variables are defined as $K_u = \lambda + 2G/3 + b^2 M$, $C_m = 1/(\lambda + 2G)$, and $c = k/\mu/(1/M + b^2 C_m)$, where λ and G are Lame constants. **Fig. 3** presents a comparison between the numerical and analytical solutions for pore pressure and vertical displacement at various time points and different depths. The comparison reveals a good agreement between the two, confirming the accuracy of our numerical model's HM coupling part. The simulation parameters are listed in **Table 1**.

1D Nonisothermal Consolidation Model. The model schematic and boundary conditions are shown in **Fig. 2b**. Unlike the Terzaghi problem, the nonisothermal consolidation model describes the compaction process of soil under the concurrent influences of stress loading and heating. The analytical model assumes that, at the loading moment, there is insufficient time for soil deformation, leading to zero initial displacement and an initial pore pressure equivalent to the externally applied force. The boundary conditions for the seepage and

Parameter	Magnitude	Description
L	15 m	Model size
p_L	1.0×10^4 Pa	Magnitude of loading force
ϕ	0.375	Porosity of the soil
k	1,000 md	Permeability
E	0.1 GPa	Elastic modulus
b	1.0kg/m^3	Biot coefficient
ρ	1000 kg/m^3	Density of the water
μ	1.0 mPa·s	Viscosity of the water
v	0.25	Poisson's ratio of the soil
c_f	4.4×10^{-10} Pa^{-1}	Compressibility of the water
c_s	1.0×10^{-11} Pa^{-1}	Compressibility of the particle

Table 1—Parameters used for the Terzaghi model.

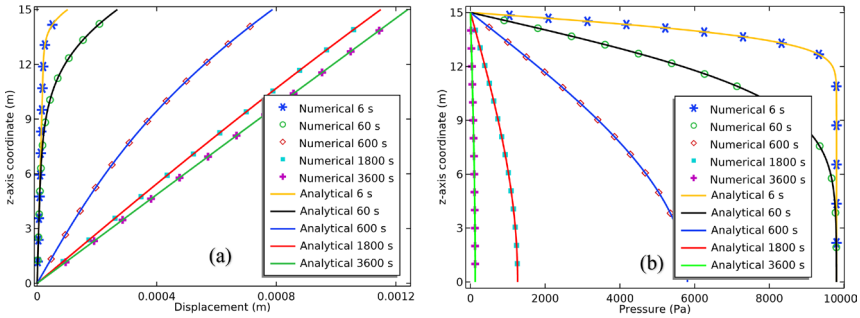

Fig. 3—Contrast between analytical and numerical results for the Terzaghi problem: (a) vertical displacement and (b) pore pressure. Solid lines represent the analytical solutions, and scatter points represent the numerical solutions.

displacement field in this problem are the same as those for the Terzaghi problem. Regarding the temperature field, the upper boundary is designated as a Dirichlet boundary with a prescribed temperature, while the remaining boundaries are configured as thermal insulation. Detailed formulations of the analytical solutions are outlined in the work by Bai (2005), and a similar verification work can be referred to by Shi et al. 2019 . **Fig. 4** presents a comparison of both numerical and analytical solutions for vertical displacement, temperature, and pore pressure, across various times and locations. The findings suggest a high degree of alignment between the numerical and analytical results, affirming the dependability of the THM coupling element in our numerical model. The parameters utilized for the simulation are detailed in **Table 2**.

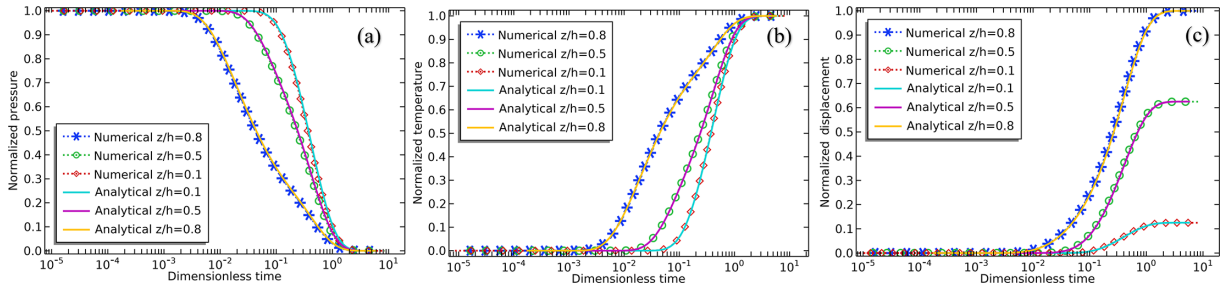

Fig. 4—Contrast between numerical and analytical solutions for the nonisothermal consolidation model: (a) normalized pore pressure; (b) normalized temperature; and (c) normalized vertical displacement. Numerical solutions are depicted using dashed lines, while analytical solutions are shown with solid lines.

Parameter	Magnitude	Description
ρ_w	1000 kg/m^3	Density of pore water
ρ_s	2600 kg/m^3	Density of soil grains
α_s	1.5×10^{-5} K^{-1}	Coefficient of thermal expansion for soil grains
α_f	2.0×10^{-4} K^{-1}	Coefficient of thermal expansion for pore water
c_w	4200 J/kg/K	Specific heat capacity of pore water
c_s	800 J/kg/K	Specific heat capacity of soil grains
ϕ	0.4	Porosity of the soil
b	1.0	Biot consolidation coefficient
K	2.07×10^{-9} m/s	Hydraulic conductivity coefficient
E	6.0×10^5 Pa	Elastic modulus of the soil
v	0.3	Poisson's ratio of the soil
k_{eff}	0.5 W/m/K	Effective thermal conductivity
p_L	100 kPa	Magnitude of applied load pressure
p_0	100 kPa	Initial pore pressure
T_0	10°C	Initial temperature
T	60°C	Externally applied temperature
h	1.0 m	Dimension of the model

Table 2—Parameters used in the nonisothermal thermal consolidation model.

Application in 3D Fault Activation Model

The present section outlines the outcomes of simulating CO_2 injection into the targeted aquifer intersected by fault. A 3D model of a multilayered geological formation has been developed. Our primary focus is on the evolution of unintended mechanical phenomena, namely, the plastic failure of the fault, the drastic change of the fault permeability, and the migration pattern of CO_2.

Fig. 5 shows a schematic diagram of the model with dimensions of 3000×3000×2500 m, aligned along the x, y, and z directions, respectively. The brown area represents two caprocks, while the blue area represents the reservoirs. Initially, the saturation of CO_2 is zero, and the pore pressure adheres to hydrostatic equilibrium. The geothermal gradient is 25°C/km with a ground temperature of 10°C, and the reservoir environment is conducive to keeping CO_2 in a supercritical state. Regarding boundary conditions, for the seepage field, the ground (top boundary) is an outflow boundary where the pressure is maintained at an atmospheric level, and the remaining boundaries are impermeable. For the displacement field, the top boundary is a free surface to move. Stress boundary conditions have been imposed on the lateral borders to simulate horizontal ground stress. It is assumed that the magnitude of stress varies linearly with the depth of the formation. Specifically, on the boundary at x = 3000 m, a horizontal load $F_x = 2250[\text{kg/m}^3] \times g_{\text{const}} \times (2500 - z) \times 0.7$ is applied. Correspondingly, on the boundary at y = 3000 m, the horizontal load changes to $F_y = 2250[\text{kg/m}^3] \times g_{\text{const}} \times (2500 - z) \times 0.6$. The remaining boundaries are roller boundaries. The temperature field features thermal insulation, with a line heat source situated at the perforated section:

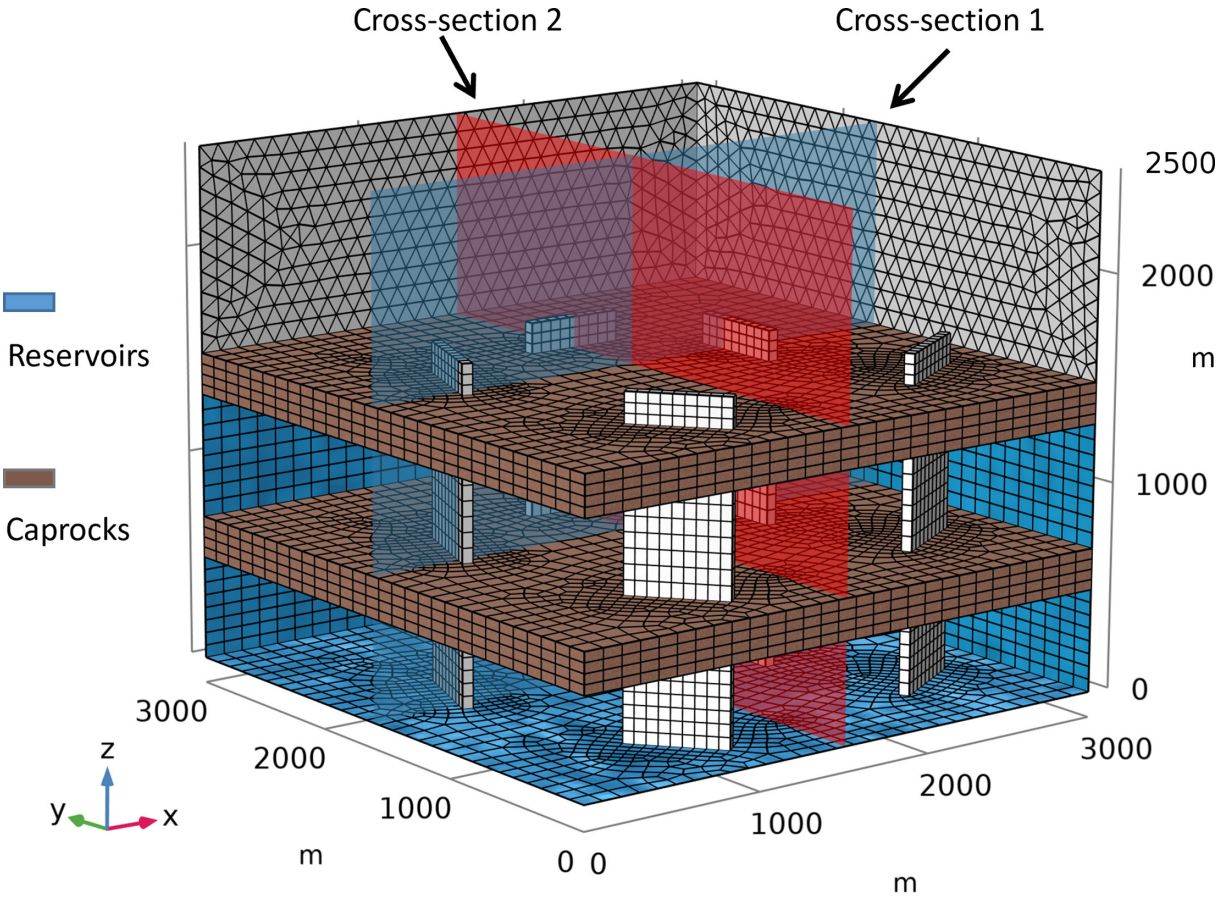

Fig. 5—Schematic diagram and grid division diagram of the 3D model, along with a simplified geometric design, based on the work of Luu et al. (2022) in the Illinois Basin. The model size is 3000×3000×2500 m. The brown area represents two caprocks, while the blue area represents the reservoirs, with a generic set of vertical faults included. Two transparent sections are marked for detailed observation.

$$Q_l = C_{p_{CO_2}} \times M_l \times (T_{\text{inj}} - T), \tag{15}$$

where Q_l represents the line heat source intensity; $C_{p_{CO_2}}$ is the isobaric heat capacity of CO_2; M_l represents the mass flow rate per unit length, defined as $M_l = M_{\text{inj}}/L_{\text{inj}}$; M_{inj} is the total injection rate; L_{inj} is the length of the perforated section at the wellbore; T_{inj} denotes the injected fluid's temperature; and T represents the ambient temperature at the perforated section. **Table 3** outlines the parameters used for this model. The system we simulate here is a vertical well, with a perforated section totaling 50 m in length, located within a depth from 2250 m to 2300 m. Note that we do not conduct a 3D structure of the wellbore, as the wellbore diameter is significantly smaller compared with the overall field size. A 3D geometric modeling of the wellbore structure would result in poor mesh quality, so we opt to use a line heat source as a substitute, implemented through the well interface built in COMSOL Multiphysics®.

	Parameter	Value	Description
Common parameters of rock mass	E	20 GPa	Elastic modulus
	v	0.25	Poisson's ratio
	b	1.0	Biot coefficient
	ρ_s	2400 kg/m^3	Density of solid matrix
	c_s	850 J/kg/K	Specific heat capacity of solid matrix
	k_s	3.0 W/m/K	Thermal conductivity of solid matrix
	α_m	2.0×10^{-5} K^{-1}	Thermal expansion coefficient of rock
	E_n	1.0×10^3 (Guglielmi et al. 2015)	Enhancing factor on fault permeability
	A	10 (Kanin et al. 2024)	Amplify factor on volumetric strain
	n	10 (Yehya et al. 2018)	Index required for permeability model
	c	0.5 MPa	Cohesion
	ϕ	30°	Internal friction angle
Parameters of brine	ρ_w	1050 kg/m^3	Density of brine
	μ_w	1.0 mPa·s	Dynamic viscosity of brine
	χ_w	4.4×10^{-10} Pa^{-1}	Compressibility of brine
	k_w	0.6 W/m/K	Thermal conductivity of brine
	c_w	4200 J/kg/K	Specific heat capacity of brine
Parameters of CO_2	M_{inj}	100 kg/s	Injection rate of CO_2
	T_{inj}	10°C	Temperature of injected CO_2
Capillary pressure parameters	p_{ec}	200 kPa (Class et al. 2009)	Entry capillary pressure
	m_{vG}	0.5	Constitutive constant of the v-G model
	l_{vG}	0.5	Constitutive constant of the v-G model
	s_{rw}	0.2	Residual saturation of brine
	s_{rn}	0	Residual saturation of CO_2
Heterogeneity parameters of strata	Reservoirs	$\phi = 0.2 \;\; k = 1.0 \times 10^{-13}$ m^2	Porosity and permeability of reservoirs
	Caprocks	$\phi = 0.01 \;\; k = 1.0 \times 10^{-20}$ m^2	Porosity and permeability of caprocks
	Upper aquifer	$\phi = 0.1 \;\; k = 1.0 \times 10^{-15}$ m^2	Porosity and permeability of the upper aquifer
	Fault	$\phi = 0.1 \;\; k = 1.0 \times 10^{-17}$ m^2	Initial porosity and permeability of the fault

Table 3—Parameters of the 3D fault activation model.

Fig. 6 illustrates the entire trajectory of CO_2 plume transportation, elucidating how the dispersal scope of these plumes progressively expands over time. It is observed that CO_2 migrates upward along the fault gradually. However, the faults initially possessed extremely low permeability, theoretically impeding the upward flow of CO_2 plumes along them. The occurrence of CO_2 seepage along the fault implies a transition from its original low-permeability state to a permeable one, indicating fault activation. Notably, our model posits the lateral boundaries of the seepage field as impermeable, leading to the accumulation of pore pressure. Consequently, faults embedded within the reservoir gradually reactivate, enabling CO_2 to migrate along these fault pathways and permeate into the overlying aquifer. This will be further confirmed by the subsequent evolution of fault permeability and pore pressure within the faults. Additionally, we observe that CO_2 gradually accumulates at the interface between the reservoir and caprock, forming areas with high volume fractions.

Fig. 7 provides a comprehensive visualization of the progressive failure mechanism of the faults. In the initial stage, the faults maintain an elastic state characterized by the absence of plastic strain. However, as fluid injection is introduced into the fault system, the stress state begins to shift dramatically. The injected fluid alters the pressure and stress distribution within the fault zones, causing the stress levels to gradually exceed the material's yield limit. This critical point (cf. **Fig. 7**, t = 0.6 a) marks the onset of plastic deformation and failure process. The failure areas, initially confined to localized regions, gradually propagate and extend to encompass all fault zones. This expansion of failure zones reflects the progressive weakening and eventual loss of integrity within the fault structure. The significant differential distribution observed in **Fig. 7** indicates that different regions of the fault zone experience varying degrees of plastic deformation, highlighting the heterogeneity of the fault's response to stress and fluid injection.

Fig. 8 shows the development process of fault permeability. Initially, the fault is not activated and thus maintains a low permeability. As pore pressure gradually accumulates, the material undergoes failure and the corresponding points are activated. Due to the discontinuous permeability constitutive model that we adopted, the permeability in these corresponding zones will experience a jump after fault activation, resulting in a significant permeability perturbation between the activated and inactive areas. Over time, the original low-permeability faults have developed into high-permeability channels. At the same time, a positive correlation with plastic strain can also be observed, and the more obvious the damage, the higher the permeability in these areas.

Fig. 9 shows the evolution process of the temperature field. In this 3D case study, we have adopted a commercial injection rate of 100 kg/s, approximately 3.15 Mt/yr. This rate is strategically chosen based on a comparison of existing commercial-scale CO_2 storage projects worldwide. For instance, StatoilHydro has been pioneering the capture and sequestration of CO_2 since 1996, extracting 1 Mt CO_2/yr from "a natural gas platform in the Sleipner Field (North Sea)," and subsequently injecting it into a sandstone reservoir (Schrag

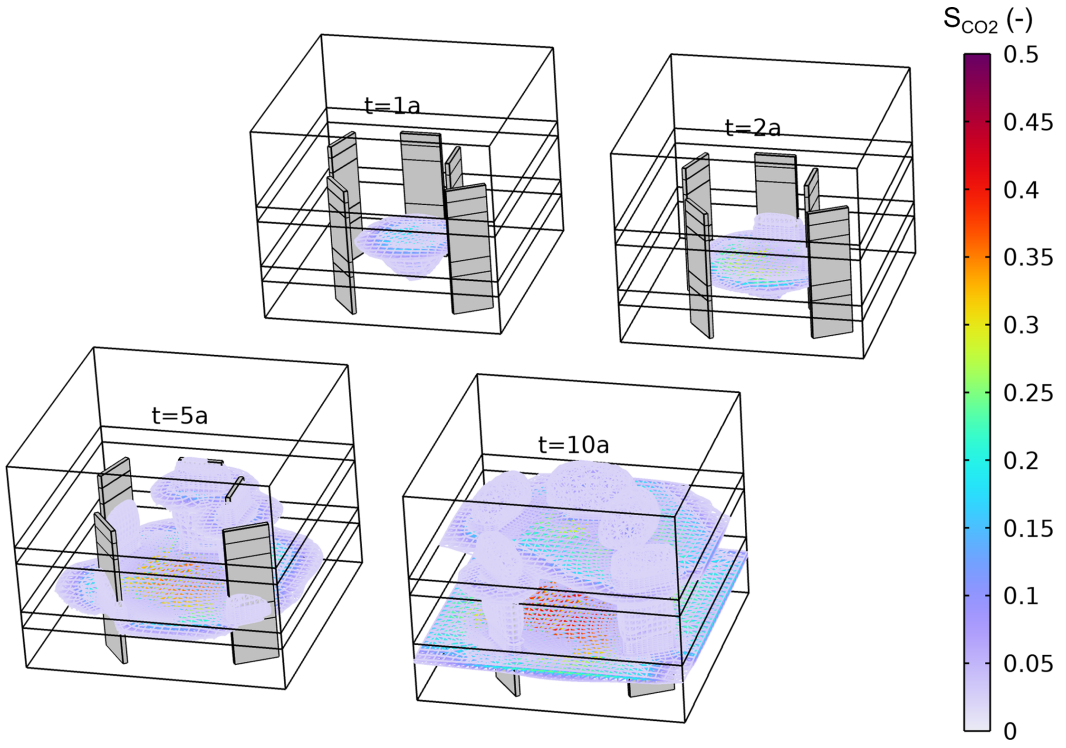

Fig. 6—Transport process of CO_2 plume along activated faults. The faults are marked in gray.

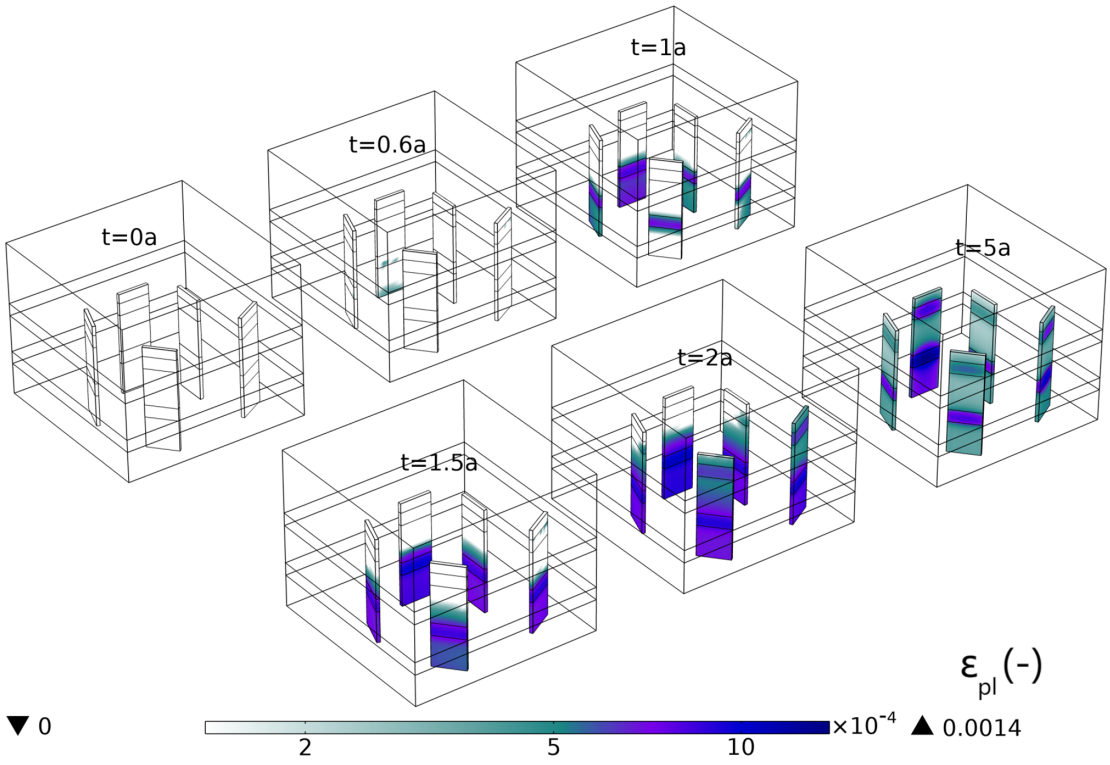

Fig. 7—Plastic failure process of faults and the depth of color indicate the magnitude of plastic strain.

2009). In addition, Norwegian authorities have advocated for the establishment of two gas-fired power stations equipped with full-scale CCS technologies at Kårstø and Mongstad, capable of producing 1.1 Mt and 2.2 Mt CO_2/yr, respectively (Eigestad et al. 2009). Our selected injection rate of 3.15 Mt/yr aligns with these industry benchmarks, ensuring that our simulations remain grounded in practical, commercially viable considerations. **Fig. 9** reveals the gradual expansion of the low-temperature area over time. Notably, the low-temperature zone is concentrated near the injection well without contacting the faults, extending approximately 400 m under the commercial injection rate. Reports by Vilarrasa et al. (2014) align with this observation, indicating a cooling region of up to a few hundred meters

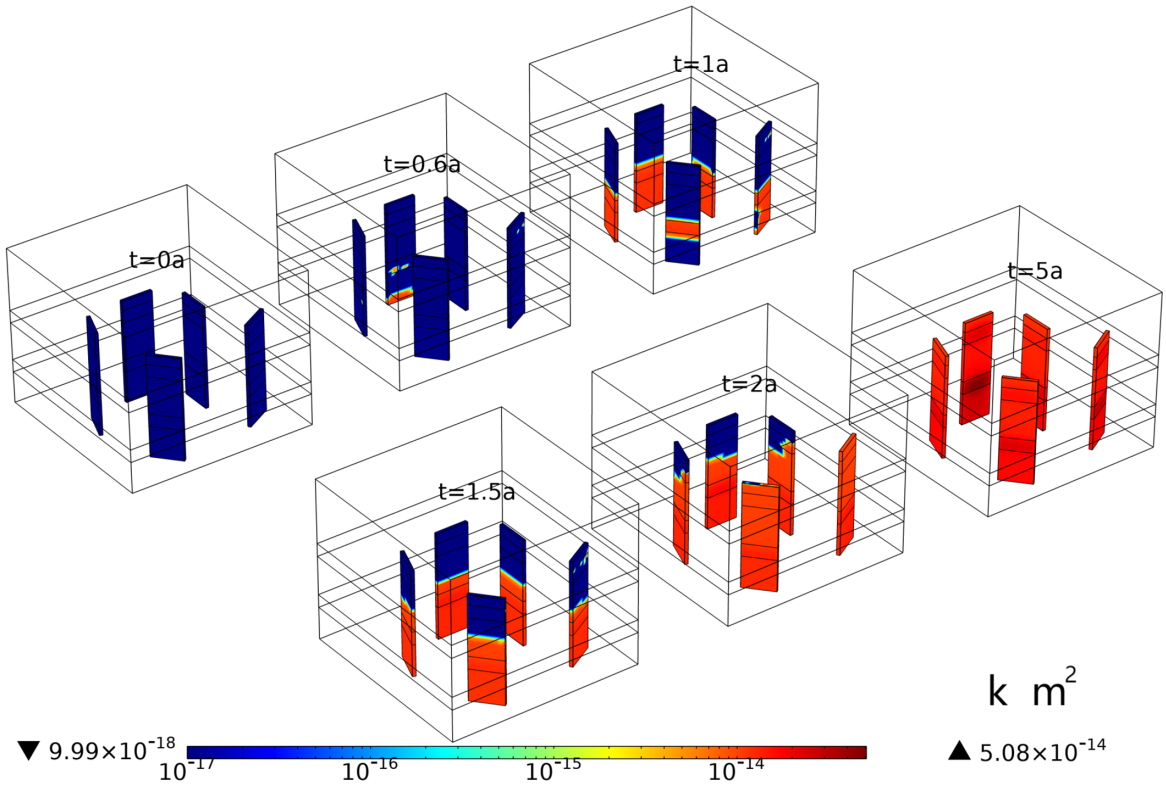

Fig. 8—Evolution process of fault permeability.

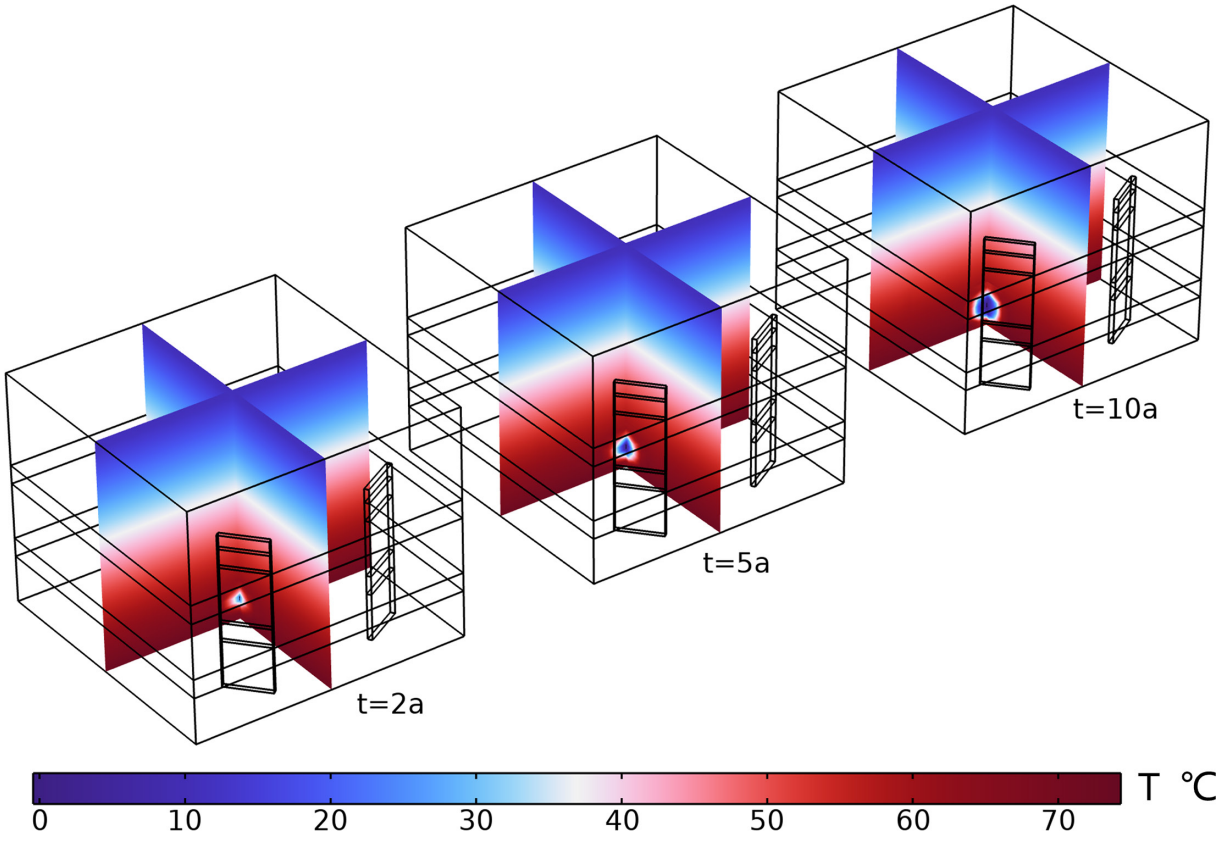

Fig. 9—Evolution of the temperature field.

after decades of megatonne-scale CO_2 injection. Overall, the expansion range of the low-temperature zone is relatively limited, contrasting significantly with the vast escape range (**Fig. 6**). We know that the cooling effect can reduce rock's effective stress and potentially

induce seismic activity. This limited cooling effect, which is advantageous for CO_2 sequestration, will have no direct impact on faults, provided they are not near the injector. This unique temperature field pattern during CO_2 sequestration in saline aquifers contributes to the long-term safety of CCS.

Fig. 10 shows the evolution process of the pore pressure field on two different cross sections. Cross Section 1 passes through two faults. Because the injection well is located in the lowest reservoir, it can be seen that the increase in pore pressure at the lowest reservoir is the most significant. Subsequently, through activated faults, the pore pressure gradually spreads to the middle reservoir and finally to the overlying aquifer. Two obvious pressure propagation fronts can be seen at the junction of faults and caprocks. Meanwhile, because of the extremely low permeability of the caprock, it is hard for fluids to penetrate it, and the fluid pressure inside the caprock almost maintains the initial pore pressure distribution, which is not significantly increased compared with the surrounding reservoir area. The pattern of Cross Section 2 is similar to that of Cross Section 1. Because Cross Section 2 only intersects with one fault, and only one pressure front edge is shown on the pressure map, the location of the faults can be clearly determined based on the position of the pressure front.

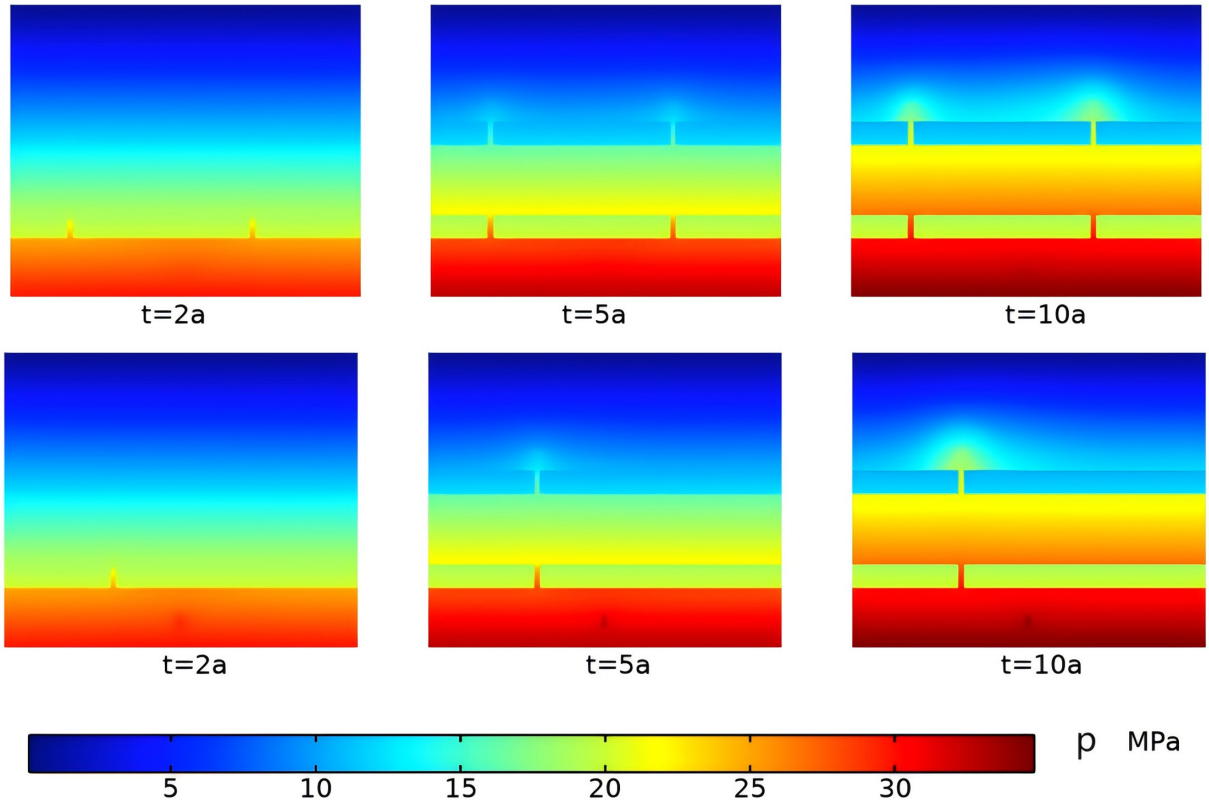

Fig. 10—Snapshots of pore pressure field for Cross Section 1 (upper) and Cross Section 2 (lower). The position of the sections can be identified in Fig. 5. The pressure front formed by fluid intrusion into the upper aquifer can be clearly reflected in the pressure map.

Fig. 11 shows the distribution of volumetric strain on two different cross sections. In the early stage of fluid injection, the fault has not yet been activated, and the volumetric strain within the fault has not yet developed. Due to the thermal effect, there is just a significant negative volumetric strain around the injection well, and the negative volumetric strain zone continues to expand over time. As pore pressure gradually increases, faults begin to experience plastic failure, leading to significant plastic deformation, with a strain amplitude significantly higher than that of the surrounding area. The strain distribution map clearly shows the positions of the activated faults.

The aforementioned pattern arises from closed boundaries, where lateral boundaries are set as impermeable, constituting a prerequisite for establishing a pressure-contained environment within the system. In this scenario, we have observed both the gradual failure of faults and significant CO_2 leakage along them (cf. **Figs. 6 and 8**). This evolutionary pattern presents a conservative assessment, particularly revealing the ultimate fate and leakage pathway of CO_2 in the worst-case scenario. A real-world example of implementing an impermeable or symmetrical boundary (mathematically equivalent) is the CO_2 sequestration project in the Snøvhit field, where a symmetrical fault structure contributed to a discernible ground uplift from the injected CO_2 (Hansen et al. 2013; Rinaldi et al. 2015; Meguerdijian and Jha 2021). However, due to the inherent uncertainty of geological formations, it is acknowledged that not all strata have such symmetrical geometry and boundary conditions. Consequently, we believe that it is necessary to expand the simulation work to a more general situation. Herein, we compare the results of closed boundaries with those of more general open boundaries, where hydrostatic pressure conditions are applied to the lateral boundaries of the model domain. **Fig. 12** depicts the temporal evolution of CO_2 plumes under open boundary conditions, highlighting a stark contrast in the migration patterns compared with those observed in **Fig. 6**. Notably, in this scenario, the fault remains dormant, preventing the upward leakage of CO_2 along it. In contrast, the CO_2 plume adeptly bypasses the low-permeability faults it encounters. Consequently, the CO_2 flows unimpeded in the horizontal direction, directly exiting the model domain through lateral boundaries, resulting in a significant accumulation of CO_2 beneath the overlying caprock. The growth pattern of pore pressure in **Fig. 13** further reveals the underlying reasons.

Fig. 13 illustrates the incremental pattern of pore pressure under the open boundary. It shows that the increase in pore pressure is marginal within the bottom reservoir. At $t = 2$ a, the increment in pore pressures around the injection well reaches approximately 1.0 MPa at an industrial-scale injection rate (i.e., 3.15 Mt CO_2/yr). Two noteworthy trends are observed: First, the overall pore pressure field

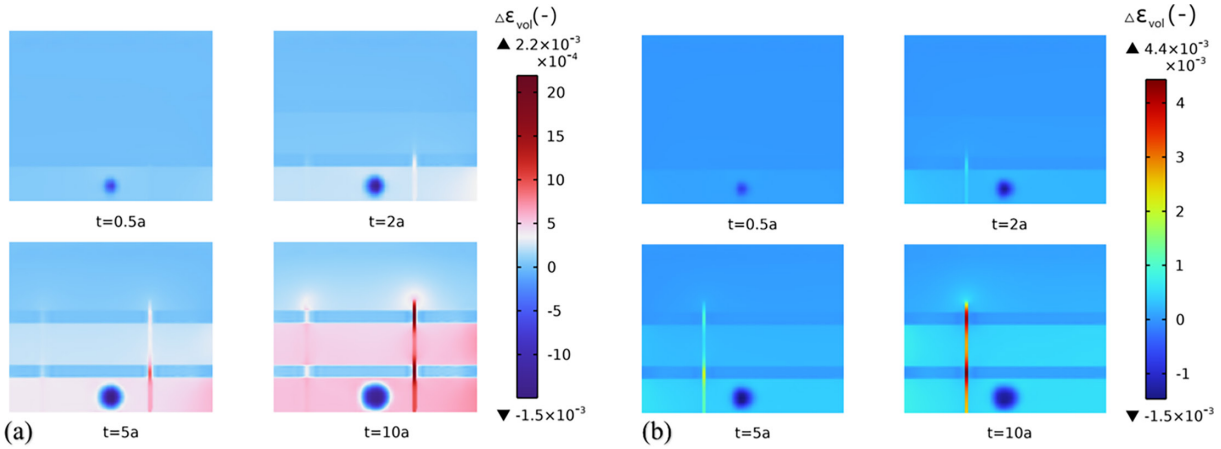

Fig. 11—Snapshots of volumetric strain at various times for (a) Cross Section 1 and (b) Cross Section 2. Due to plastic deformation, the volumetric strain within the faults is significantly higher than the surrounding area.

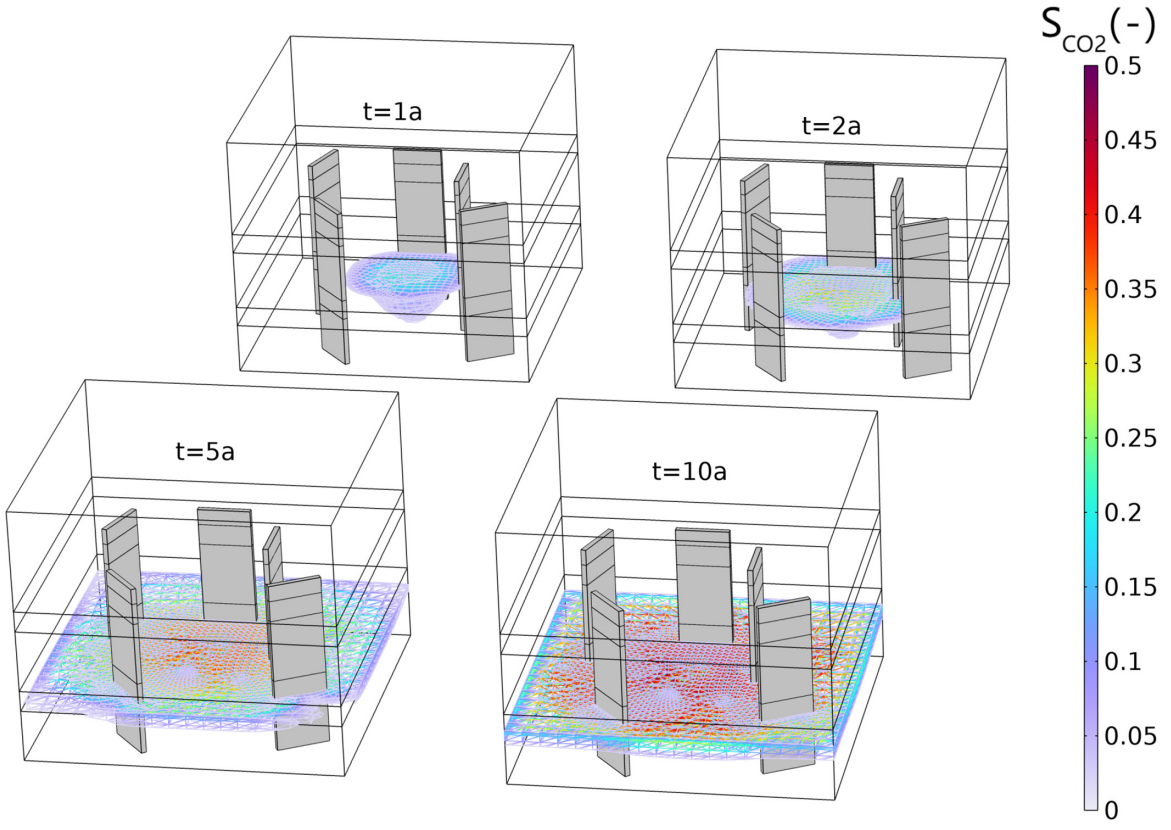

Fig. 12—Development of CO_2 plumes over time under open boundary conditions.

dissipates over time; second, the pore pressure increase becomes increasingly limited as the distance from the injection well increases, with only about 0.2–0.5 MPa transmitted to the faults at t = 10 a. As long as the fault is not adjacent to the injection well, the stress state of the fault evaluated under the open boundary is relatively safe. The pressure front within the faults is barely discernible under the open boundary, starkly contrasting with the significant pressure intrusion depicted in **Fig. 10**.

Herein, we introduce a dimensionless pressure to quantify changes in pore pressure; the dimensionless reservoir pressure perturbation is defined as (Zhao and Jha 2022)

$$\Delta p_{rd} = \left| \frac{p_{\text{res}}}{p_{\text{res},0}} - 1 \right|, \tag{16}$$

where p_{res} is the average reservoir pressure defined as $p_{\text{res}} = \int pdV/V_{\text{res}}$; V_{res} is the volume of the target reservoir; and $p_{\text{res},0}$ represents the initial reservoir pressure before disturbed.

Fig. 14a depicts the bottomhole pressure curves under two distinct boundary conditions. At the initial injection moment, there is an instantaneous surge in the wellbore pressure in both cases. However, under the closed boundary, the pore pressure at the wellbore

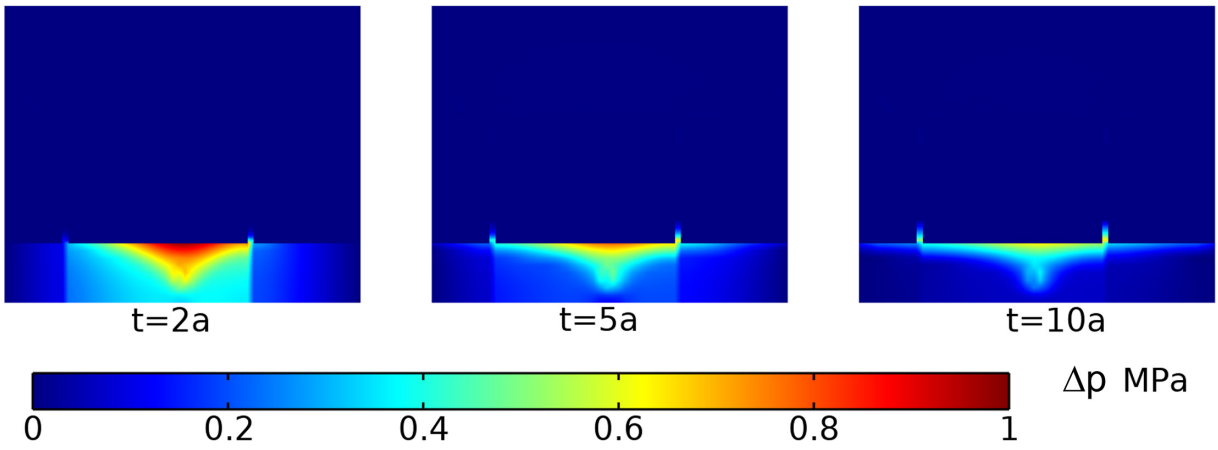

Fig. 13—Increment of pore pressure under open boundary conditions.

continues to escalate, reaching almost 10 MPa after 10 years, creating unfavorable conditions for fault activation. In contrast, the pore pressure rapidly stabilizes under the open boundary, with an increase of merely 1–2 MPa, indicating a safer storage environment. Furthermore, **Fig. 14b** illustrates the reservoir pressure perturbations under two scenarios, offering a more precise quantification of their respective cumulative pressure effects. Specifically, under the closed boundary condition, the reservoir's average pressure undergoes a marked escalation, soaring to 39% after long-term industrial-scale injection. Conversely, under the open boundary condition, the reservoir pressure perturbation experiences a mere 0.6% increase, implying that the limited increase in pore pressure is insufficient to trigger fault slippage. This stark contrast underscores the paramount importance of boundary conditions in assessing the stress state of faults, which in turn influences the prediction of CO_2 plume migration directions. Consequently, it necessitates a thorough exploration of the distribution of underground low-permeability structures, aiming to clarify their extent as precisely as possible and ascertain whether effective fluid trapping zones can be formed in the fully 3D site model, which greatly helps us enhance the predictive ability of CCS activities.

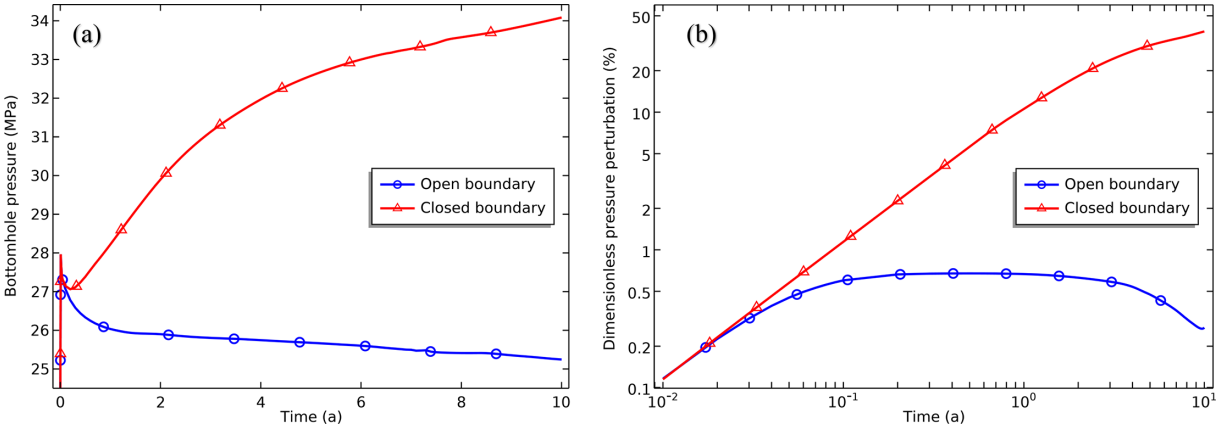

Fig. 14—Quantification of bottomhole pressure and average reservoir pressure: (a) bottomhole pressure curves under two boundary conditions and (b) dimensionless reservoir pressure disturbance under two boundary conditions.

Discussion

The total degree of freedom of the above 3D model is 629,832. It is convenient to tackle such large-scale and highly nonlinear problems using the fully coupled scheme in COMSOL. We run this model on a workstation equipped with an Intel® Xeon® Gold 6240 R CPU @ 2.40 GHz (X2), with a cost of about 3,890 minutes to complete. However, fully coupled algorithms are still expensive when dealing with large-scale and strongly nonlinear multiphysics problems (Settari and Mounts 1998; Mikelić and Wheeler 2013; Kim et al. 2013). We attempt to find a robust and efficient decoupling strategy to tackle such multiphase, nonisothermal, and strongly nonlinear THM problems, particularly those involving fault activation and accompanied by step changes in material properties. When dealing with the three physical fields involved—seepage, heat transfer, and solid deformation—a total of $A_3^2 = 6$ types of solving sequences can be combined on a field-by-field basis, and we explore the six decoupling strategies exhaustively. Given that all fields in this model are constructed on a unified platform, a significant advantage is our capability to flexibly adjust the solving sequence of the physical fields within COMSOL, enabling us to test the stability and convergence rates of the various decoupling strategies.

When utilizing a decoupling algorithm to solve multifield equations in COMSOL, two convergence plots can be obtained. One is the segregated convergence plot, which is **Fig. 15** provided here, illustrating the relative error evolution of individual fields during the computation. The other is the total convergence plot, evaluating the overall performance of the decoupling strategy and depicting the history of stepsize over time. In **Fig. 15**, the display order of field variables in the legend corresponds to the decoupling order. Specifically, in **Fig. 16a**, the legend sequence is organized according to pressure, temperature, and displacement, indicating that the pressure field is solved first, followed by the temperature field, and finally the displacement field. The same logic applies to other legends.

In **Fig. 15**, the ordinate represents the relative error, while the abscissa indicates the total number of iterations required to complete the entire simulation calculations [i.e., the cumulative number of Newton iterations performed from the initial time ($t = 0$) up to the current moment]. **Fig. 15** implies that a smaller value on the abscissa indicates a faster completion of the solution. For instance, in the pressure→-temperature→displacement (P-T-D) sequence **(Fig. 15a)**, to complete a 10-year simulation, the solver recorded a total of approximately 280 iterations. In contrast, under the D-P-T sequence **(Fig. 15f)**, the same simulation required around 700 iterations, clearly indicating the differences in efficiency between different decoupling sequences. **Table 4** further provides the physical completion time of model solving under different sequences.

Solution Strategy	Fully Coupling	P-T-D Sequence	P-D-T Sequence	T-P-D Sequence	T-D-P Sequence	D-T-P Sequence	D-P-T Sequence
Total time consumption	2 days 16 hours 50 minutes	1 hours 51 minutes	2 hours 30 minutes	2 hours 38 minutes	2 hours 56 minutes	2 hours 51 minutes	3 hours 11 minutes

Table 4—Completion time of the numerical model solving under different solution strategies.

On the other hand, the patterns depicted in **Fig. 15** reveal pronounced stability disparities arising from distinct decoupling sequences. Taking the P-T-D sequence **(Fig. 15a)** as an example, after approximately 50 total iterations, the subsequent convergence curves follow a monotonically decreasing trend. In contrast, the P-D-T sequence (**Fig. 15b**) requires approximately 150 iterations before the numerical system stabilizes. Our numerical models all exhibit a certain degree of error oscillations at the initial running stage under various decoupling sequences. Differently, under some preferred sequences (as illustrated in **Figs. 15a and 15b**), these initial oscillations tend to stabilize and gradually diminish as the solution progresses. Conversely, under less favorable sequences (as shown in **Figs. 15c–15f**), these error oscillations not only fail to diminish but may even intensify as the solution continues.

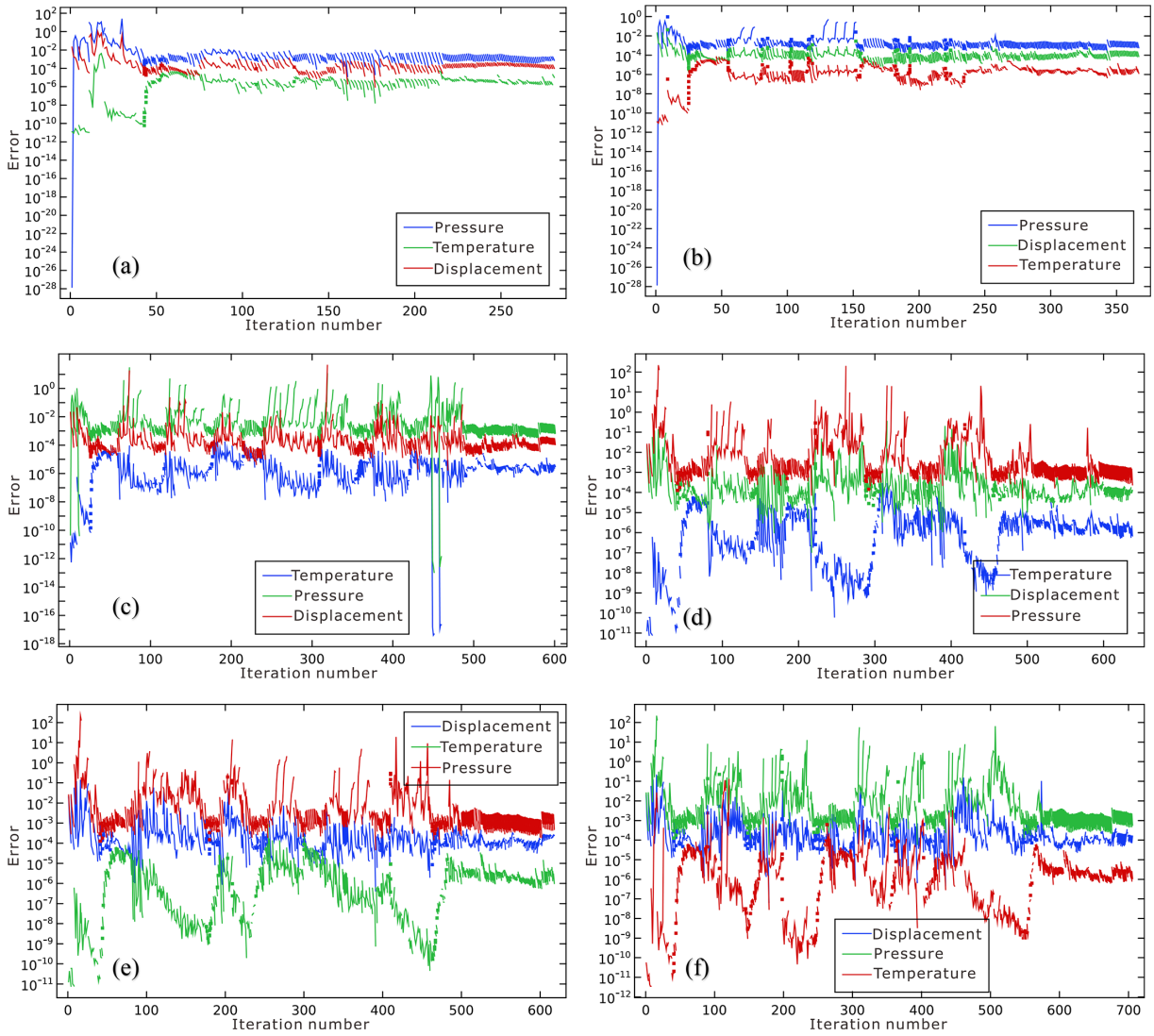

Fig. 15—Relative error curves of individual fields under different decoupling (segregated) strategies. The display order of field variables in the legend corresponds to the decoupling order.

Notably, the curves following the solution sequences of P-T-D field and P-D-T field exhibit the weakest error oscillations, as illustrated in **Figs. 15a and 15b**, respectively. Among these two, the stability of the P-T-D sequence emerges as the superior choice. In terms of the above two sequences' stability disparities, a qualitative reason is given from the perspective of the equations. We believe that, for coupled THM problems, although all three fields are strongly coupled (meaning that underlying physical interactions such as heat transfer, seepage, and solid deformation occur simultaneously), the priority of effects among fields may not be the same. Starting to solve for the displacement field before determining the temperature field potentially introduces inaccuracy. Considering the explicitly included term for thermal stress in Eq. 8, this sequence may lead to cumulative errors in thermal stress calculations, resulting in stronger oscillations in **Fig. 15b** compared with **Fig. 15a**. In contrast, the strain energy released by structural deformation is ignored, it can be considered that structural deformation does not directly affect the temperature field, and correspondingly, the energy Eq. 9 does not explicitly incorporate terms related to structural displacement. Overall, the degree of direct influence between the displacement field and the temperature field is different. Furthermore, **Figs. 15c–15f** illustrate the remaining four decoupling schemes, revealing that their stability is significantly compromised, suggesting ineffective decoupling strategies.

Another intriguing phenomenon is that when the pressure field is solved first, there is a pronounced transient surge resulting from the sudden disturbance of the injected fluid on the initial hydrostatic pressure field (cf. **Figs. 15a and 15b**). This surge can readily lead to stability issues at the initial time, causing the equation system to collapse immediately upon solving. By solving other fields (such as temperature or displacement) first, the initial stability problems can be effectively mitigated (cf. **Figs. 15c–15f**). However, this approach may contradict the underlying physical mechanisms of these field equations, potentially inducing worse stability issues. To overcome the initial stability problems induced by solving the pressure field first, here we employ a piecewise function for setting the injection flow rate (i.e., $M_{\mathrm{inj}}(t) = \frac{1-\mathrm{sgn}(t-a)}{2}\left(M_{\max}/a \times t\right) + \frac{1-\mathrm{sgn}(t-a)}{2} M_{\max}$). Specifically, the maximum injection rate ($M_{\max}$ = 100 kg/s) is achieved after a = 0.5 days, providing a short transitional period for the entire physical system to start, thus avoiding a step change from 0 to 1.

Fig. 16 presents the total convergence plots of various decoupling strategies, depicting the history of stepsize over time. The vertical axis represents the reciprocal of the stepsize, and the horizontal axis denotes the cumulative number of timesteps taken to complete the 10-year simulation journey. **Fig. 16** reflects the temporal oscillation effect of various decoupling strategies. An ideal convergence curve should exhibit a monotonically decreasing trend over time, implying that the reciprocal of the stepsize decreases monotonically, meaning the stepsize itself increases monotonically. As the computation progresses, the adaptive timestepping method can employ wider stepsizes,

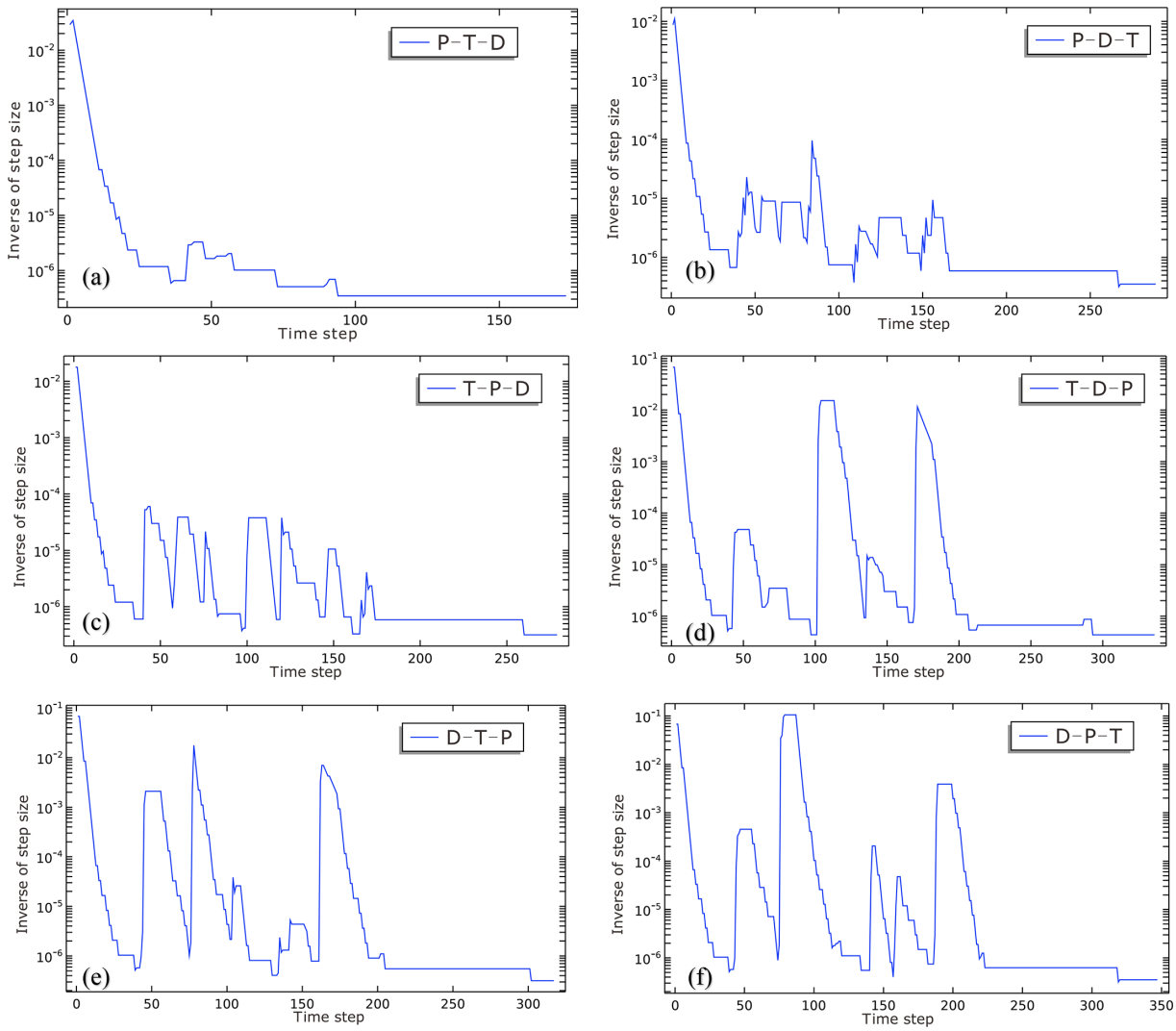

Fig. 16—Historical curves of step size under various decoupling (segregated) sequences, with P-T-D denoting a sequence where the pressure, temperature, and displacement fields are solved successively. Other legends follow similarly.

corresponding to higher computational efficiency. If the adaptive timestepping method constantly adjusts the stepsize up and down, it will waste more time finding solutions and also reflect insufficient numerical stability.

Comparing the oscillation amplitudes of different decoupling strategies depicted in **Fig. 16**, the P-T-D sequence (cf. **Fig. 16a**) stands out with significantly weaker temporal oscillation effects, characterized by a nearly monotonically decreasing curve. In contrast, under other sequences, the solver needs to continuously adjust the stepsize to obtain solutions when crossing time intervals, indicating a greater difficulty in finding the true solution and reflecting inadequate stability. Overall, the P-T-D decoupling sequence yields the most robust convergence curve and demonstrates the fastest convergence speed among all strategies. For instance, the P-T-D strategy completes the 10-year simulation journey in just about 170 steps, whereas the D-P-T strategy requires 350 steps to finish the same journey. Moreover, these graphs reveal a notable feature: Scenarios exhibiting significant oscillations (cf. **Figs. 16d–16f**) share a commonality. Specifically, the displacement field is solved before the pressure field. In contrast, the amplitudes for the other three groups are notably weaker.

Given that structural deformation is significantly constrained by pore pressure, attempting to solve for the displacement field first, without obtaining a more precise pressure solution, can lead to the accumulation of errors in effective stress. Furthermore, the cumulative errors in displacement can compromise the judgments regarding fault activation states, which in turn correspond to vastly different permeability properties, eliciting instability within the seepage field and contributing to the observed significant oscillations. Initiating displacement calculations without an accurate pressure solution inherently relies on pressure approximations, potentially overlooking complex pressure-deformation couplings. We believe the sequence of pressure-to-displacement, as opposed to displacement-to-pressure, is preferred because it better aligns with the fundamental physics governing the problem. By first solving for the pressure field, this approach ensures that the displacement field is based on an accurate representation of the pressure-induced stress state, minimizing error accumulation and improving the overall accuracy and stability of the simulation.

It should be pointed out that although the P-T-D sequence mentioned above is relatively robust and efficient compared with the other five sequences, this does not necessarily imply it is the sole feasible solution for solving such nonlinear multiphase and multifield coupling challenges. In fact, upon further examining the error magnitude of the P-T-D sequence depicted in **Fig. 15a**, we discover the error order in terms of pressure and displacement can reach 0–1 within the first approximately 50 iterations. Such a relative error may be considered too large.

In our previous comparison of the convergence behavior under different sequences, we speculate that the priority of influence between fields may vary. However, quantifying one field's priority or influence degree on another is not straightforward. When the relative influence degree between fields is unclear and difficult to assess, a prudent approach is to bundle and solve for the fields with significant impacts together, such as the pressure and displacement fields, which exhibit greater influence in our model. Consequently, we conduct an additional comparison of the model's convergence behavior under a PD-T sequence. Indeed, existing research has shown a strong coupling relationship between the pressure and displacement fields (Cui and Wong 2022).

Fig. 17 illustrates the convergence behavior of the model under the PD-T sequence. We observe that, when the displacement and pressure fields are solved simultaneously, their relative errors range from −2 to −4, with a significant reduction during the model's initial iterations (vs. **Fig. 15a**). This difference in the PD-T and P-T-D sequences reflects a strong coupling relationship between the displacement and pressure fields, implying potential inaccuracies in decoupling methods. Consequently, further verification of the reliability of the P-T-D sequence is required.

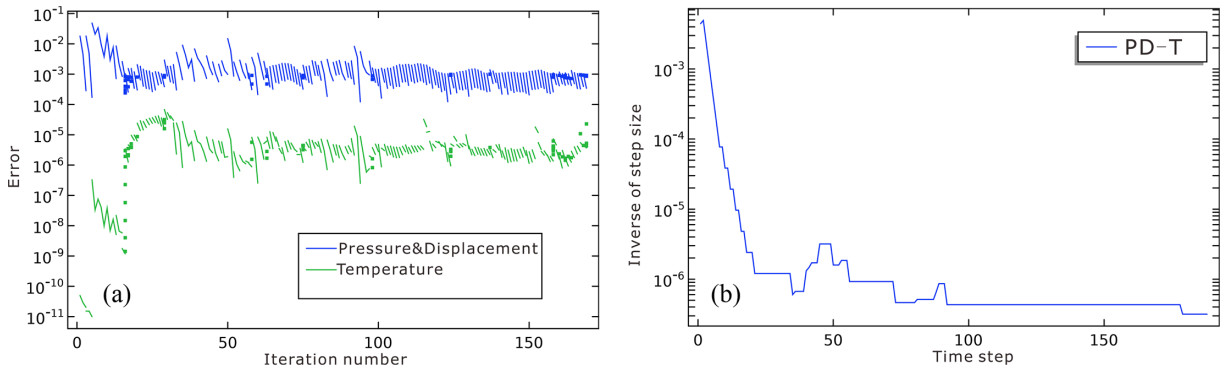

Fig. 17—Convergence performance of the numerical model under PD-T sequence: (a) the relative error curves and (b) historical curves of step size.

One of the most straightforward methods to verify accuracy is by comparing the results obtained from two sequences. **Fig. 18** contrasts the outcomes of the field variables across various spatial points for the P-T-D and PD-T sequences, revealing a close agreement between them. This confirms that the P-T-D decoupling method does not significantly introduce errors. Meanwhile, when comparing the computational efficiency, the PD-T sequence does not exhibit more advantages. Although **Fig. 17a** indicates a reduction in the total iterations required for the PD-T scheme (vs. **Fig. 15a**), given the degree of nonlinearity in the model (which encompasses the nonlinearity of capillary pressure, material properties, and plastic deformation), a rigorous approach is adopted to ensure model convergence. Specifically, the Jacobian matrix is updated in each iteration. Despite the PD-T sequence having fewer iterations, each iteration requires a longer duration due to the need to update a larger Jacobian matrix. Consequently, these iterations are not comparable to those in the P-T-D sequence in terms of time consumption. Specifically, the PD-T scheme takes 12 hours 45 minutes to complete the transient simulation, while the P-T-D scheme only takes 1 hour 51 minutes. In summary, the P-T-D (employing a pressure→temperature→displacement sequence) iterative coupling scheme, while exhibiting superior stability and enhancing solving efficiency, also guarantees the accuracy of

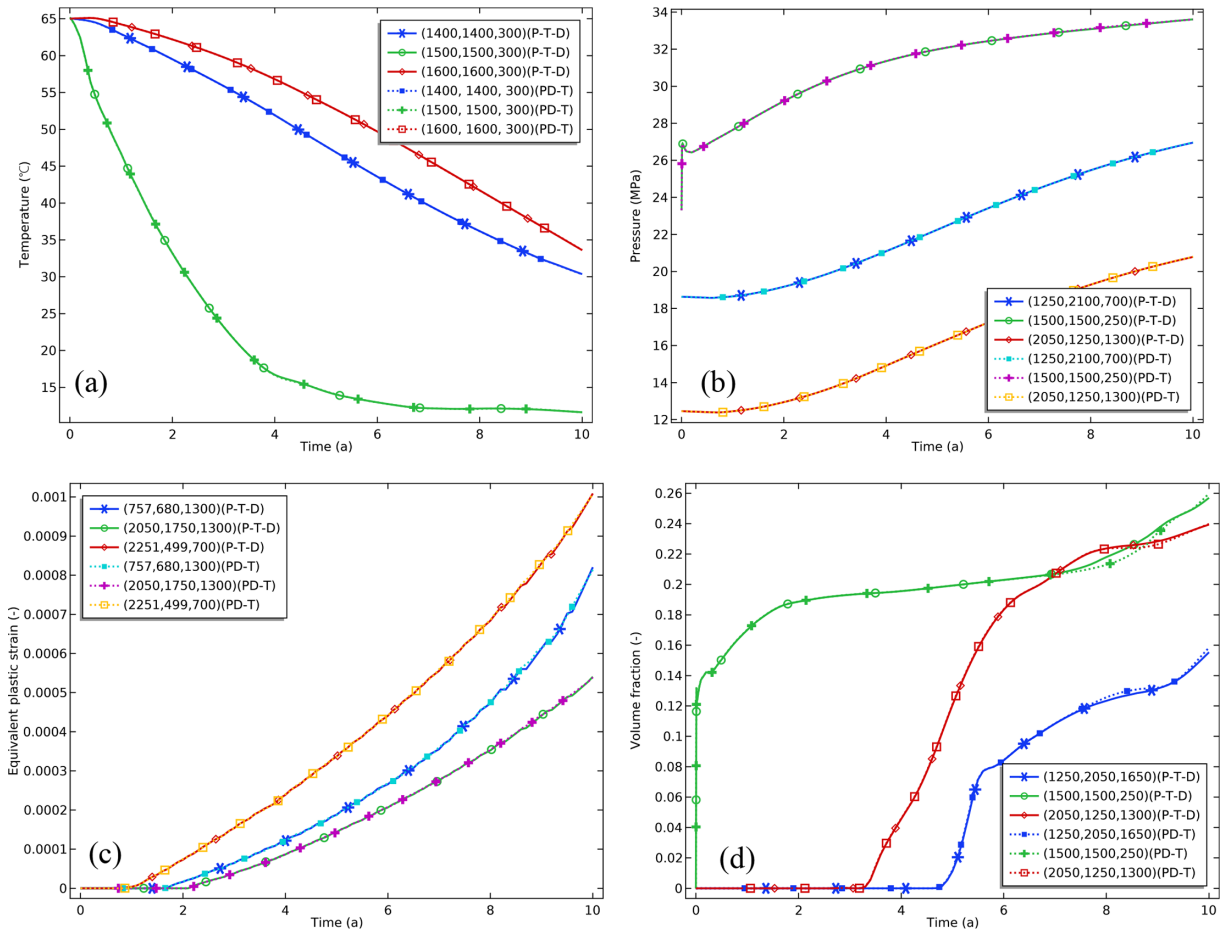

Fig. 18—Comparison of results between the P-T-D and PD-T coupled solutions: (a) temperature, (b) pore pressure, (c) plastic strain, and (d) volume fraction. The numbers in parentheses indicate the coordinates of points. The solid lines depict the P-T-D sequence, while the dashed lines depict the PD-T sequence.

the solution. Therefore, in the context of tackling such large-scale and strongly nonlinear THM problems, it provides a valuable reference for selecting a decoupling strategy.

Conclusions

The diffusion of fluid pressure along faults is considered one of the main mechanisms that induce geomechanical instability of faults. In this study, we establish an integrated multiphase THM model on COMSOL Multiphysics® that incorporates fault activation to estimate the long-term safety of CO_2 sequestration in deep saline aquifers. We have analyzed the elastoplastic failure behavior of faults and the significant changes in permeability that arise from their activation. Notably, the permeability distribution within the fault zone after activation becomes highly heterogeneous, exhibiting a strong dependence on plastic damage. Additionally, the increased permeability triggered by fault activation under closed boundary conditions significantly compromises the integrity of the caprock, providing an effective pathway for the upward migration and escape of CO_2.

Subsequently, we compare the development patterns of CO_2 plumes under closed boundary conditions and more general open boundary conditions, yielding starkly contrasting conclusions. Under closed boundaries, the average pressure disturbance in the reservoir reaches 39%, whereas it is merely 0.6% under open boundaries during a decades-long, megatonne-scale continuous injection. The closed boundary scenario points to a terrible assessment, suggesting that fault activation and CO_2 leakage are merely a matter of time due to the presence of a stable pressure-accumulation environment. In contrast, under open boundaries, the lateral migration of CO_2 is unobstructed, enabling it to bypass low-permeability faults rather than migrating upwards along them or contributing to fault activation through pressure buildup. Correspondingly, the long-term fate of CO_2 in an open boundary environment is much safer. The above phenomena underscore the necessity to delve into whether effective fluid-trapping zones can be formed in the vicinity of the faults, particularly within the context of a fully 3D real geological model where simplistic 2D axisymmetric presumptions may obscure the boundaries that allow fluid to flow out.

Furthermore, to efficiently tackle this large-scale, multiphase, and nonlinear THM problem, we focus on optimizing decoupling strategies. Six decoupling strategies are compared, and the test results reveal that the sequence in which the fields are solved significantly impacts the stability and convergence rate of the numerical model. Specifically, the sequence of first solving the seepage field, followed by the temperature field, and finally the displacement field, yields the best stability and convergence. Additionally, the accuracy of this decoupling sequence has been validated by comparing different decoupling schemes, confirming its value as a recommendation in addressing such THM problems. The varying convergence behaviors may stem from the differing priorities of influence among the field equations, while a more thorough mathematical analysis is awaited to conclusively determine this.

Credit Authorship Contribution Statement

Zijun Wei: Methodology, Investigation, Validation, and Writing - Original Draft. Ke Gao: Methodology, Funding Acquisition, Supervision, Software, and Writing - Review & Editing. Sanbai Li: Methodology, Formal Analysis, Resources, Software.

Conflicts of Interest

The authors state that no known conflicts of interest are associated with this work.

Acknowledgments

This work is funded by the Shenzhen Science and Technology Program (JCYJ20220530113612028), the National Natural Science Foundation of China (52174025), the Guangdong Basic and Applied Basic Research Foundation (2023A1515011244), and the Guangdong Provincial Key Laboratory of Geophysical High-Resolution Imaging Technology (2022B1212010002).

References

Bachu, S. 2003. Screening and Ranking of Sedimentary Basins for Sequestration of CO_2 in Geological Media in Response to Climate Change. *Environ Geol* **44** (3): 277–289. https://doi.org/10.1007/s00254-003-0762-9.

Bachu, S. 2007. Carbon Dioxide Storage Capacity in Uneconomic Coal Beds in Alberta, Canada: Methodology, Potential and Site Identification. *Int J Greenh Gas Control* **1** (3): 374–385. https://doi.org/10.1016/S1750-5836(07)00070-9.

Bai, B. 2005. One-Dimensional Thermal Consolidation Characteristics of Geotechnical Media under Non-Isothermal Condition. *Eng Mech* **22** (5): 186–191.

Birkholzer, J. T. and Zhou, Q. 2009. Basin-Scale Hydrogeologic Impacts of CO_2 Storage: Capacity and Regulatory Implications. *Int J Greenh Gas Control* **3** (6): 745–756. https://doi.org/10.1016/j.ijggc.2009.07.002.

Brooks, R. H. and Corey, A. T. 1966. Properties of Porous Media Affecting Fluid Flow. *J Irrig and Drain Div* **92** (2): 61–88. https://doi.org/10.1061/JRCEA4.0000425.

Caine, J. S., Evans, J. P., and Forster, C. B. 1996. Fault Zone Architecture and Permeability Structure. *Geol* **24** (11): 1025. https://doi.org/10.1130/0091-7613(1996)024<1025:FZAAPS>2.3.CO;2.

Cappa, F. 2009. Modelling Fluid Transfer and Slip in a Fault Zone When Integrating Heterogeneous Hydromechanical Characteristics in Its Internal Structure. *Geophys J Int* **178** (3): 1357–1362. https://doi.org/10.1111/j.1365-246X.2009.04291.x.

Cappa, F. and Rutqvist, J.. 2011. Modeling of Coupled Deformation and Permeability Evolution during Fault Reactivation Induced by Deep Underground Injection of CO2. *Int J Greenh Gas Control* **5** (2): 336–346. https://doi.org/10.1016/j.ijggc.2010.08.005.

Cappa, F., Rutqvist, J., and Yamamoto, K. 2009. Modeling Crustal Deformation and Rupture Processes Related to Upwelling of Deep CO_2-rich Fluids during the 1965–1967 Matsushiro Earthquake Swarm in Japan . *J Geophys Res* **114** (B10). https://doi.org/10.1029/2009JB006398.

Celia, M. A., Bachu, S., Nordbotten, J. M. et al. 2015. Status of CO_2 Storage in Deep Saline Aquifers with Emphasis on Modeling Approaches and Practical Simulations . *Water Resour Res* **51** (9): 6846–6892. https://doi.org/10.1002/2015WR017609.

Cappa, F., Guglielmi, Y., Nussbaum, C. et al. 2018. On the Relationship Between Fault Permeability Increases, Induced Stress Perturbation, and the Growth of Aseismic Slip During Fluid Injection. *Geophys Res Lett* **45** (20): 11,. https://doi.org/10.1029/2018GL080233.

Chin, L. Y., Raghavan, R., and Thomas, L. K. 1998. Fully-Coupled Geomechanics and Fluid-Flow Analysis of Wells with Stress-Dependent Permeability. Paper presented at the SPE International Oil and Gas Conference and Exhibition in China, 32–45, Beijing, China, 2−6 November. https://doi.org/10.2118/48857-MS.

Class, H., Ebigbo, A., Helmig, R. et al. 2009. A Benchmark Study on Problems Related to CO_2 Storage in Geologic Formations. *Comput Geosci* **13** (4): 409–434. https://doi.org/10.1007/s10596-009-9146-x.

COMSOL Multiphysics® v. 6.0. 2024 *Cn.COMSOL.Com. COMSOL AB*. Stockholm, Sweden: n. p. https://cn.comsol.com/model/two-phase-flow-in-a-porous-medium-buckleyleverett-model-61841.

Coussy, O. 2003. *Poromechanics*. John Wiley & Sons. https://doi.org/10.1002/0470092718.

Cui, X. and Wong, L. N. Y. 2022. A 3D Fully Thermo–Hydro–Mechanical Coupling Model for Saturated Poroelastic Medium. *Comput Methods Appl Mech Eng* **394**. https://doi.org/10.1016/j.cma.2022.114939.

Eigestad, G. T., Dahle, H. K., Hellevang, B. et al. 2009. Geological Modeling and Simulation of CO_2 Injection in the Johansen Formation. *Comput Geosci* **13** (4): 435–450. https://doi.org/10.1007/s10596-009-9153-y.

Faulkner, D. R., Mitchell, T. M., Healy, D. et al. 2006. Slip on "Weak" Faults by the Rotation of Regional Stress in the Fracture Damage Zone. *Nature* **444** (7121): 922–925. https://doi.org/10.1038/nature05353.

Ferronato, M., Castelletto, N., and Gambolati, G. 2010. A Fully Coupled 3-D Mixed Finite Element Model of Biot Consolidation. *J Comput Phys* **229** (12): 4813–4830. https://doi.org/10.1016/j.jcp.2010.03.018.

Fu, P., Ju, X., Huang, J. et al. 2021. Thermo-poroelastic Responses of a Pressure-driven Fracture in a Carbon Storage Reservoir and the Implications for Injectivity and Caprock Integrity. *Num Anal Meth Geomechanics* **45** (6): 719–737. https://doi.org/10.1002/nag.3165.

Fu, P., Settgast, R. R., Hao, Y. et al. 2017. The Influence of Hydraulic Fracturing on Carbon Storage Performance. *JGR Solid Earth* **122** (12): 9931–9949. https://doi.org/10.1002/2017JB014942.

Ganguli, S. S. and Sen, S. 2020. Investigation of Present-Day in-Situ Stresses and Pore Pressure in the South Cambay Basin, Western India: Implications for Drilling, Reservoir Development and Fault Reactivation. *Mar Pet Geol* **118**: 104422. https://doi.org/10.1016/j.marpetgeo.2020.104422.

Ganguli, S. S., Vedanti, N., Pandey, O. P. et al. 2018. Deep Thermal Regime, Temperature Induced over-Pressured Zone and Implications for Hydrocarbon Potential in the Ankleshwar Oil Field, Cambay Basin, India. *J Asian Earth Sci* **161**: 93–102. https://doi.org/10.1016/j.jseaes.2018.05.005.

Gasda, S. E., Stephansen, A. F., Aavatsmark, I. et al. 2013. Upscaled Modeling of CO_2 Injection and Migration with Coupled Thermal Processes. *Energy Procedia* **40**: 384–391. https://doi.org/10.1016/j.egypro.2013.08.044.

Glubokovskikh, S., Saygin, E., Shapiro, S. et al. 2022. A Small CO_2 Leakage May Induce Seismicity on A Sub-Seismic Fault in A Good-Porosity Clastic Saline Aquifer . *Geophys Res Lett* **49** (12). https://doi.org/10.1029/2022GL098062.

Guglielmi, Y., Cappa, F., and Amitrano, David. 2008. High-Definition Analysis of Fluid-Induced Seismicity Related to the Mesoscale Hydromechanical Properties of a Fault Zone. *Geophys Res Lett* **35** (6). https://doi.org/10.1029/2007GL033087.

Guglielmi, Y., Elsworth, D., Cappa, F. et al. 2015. In Situ Observations on the Coupling between Hydraulic Diffusivity and Displacements during Fault Reactivation in Shales. *JGR Solid Earth* **120** (11): 7729–7748. https://doi.org/10.1002/2015JB012158.

Guglielmi, Y., Nussbaum, C., Cappa, F. et al. 2021. Field-Scale Fault Reactivation Experiments by Fluid Injection Highlight Aseismic Leakage in Caprock Analogs: Implications for CO2 Sequestration. *Int J Greenh Gas Control* **111**: 103471. https://doi.org/10.1016/j.ijggc.2021.103471.

Hansen, O., Gilding, D., Nazarian, B. et al. 2013. Snøhvit: The History of Injecting and Storing 1 Mt CO_2 in the Fluvial Tubåen Fm. *Energy Procedia* **37**: 3565–3573. https://doi.org/10.1016/j.egypro.2013.06.249.

Huber, M. L., Sykioti, E. A., Assael, M. J. et al. 2016. Reference Correlation of the Thermal Conductivity of Carbon Dioxide from the Triple Point to 1100 K and up to 200 MPa. *J Phys Chem Ref Data* **45** (1). https://doi.org/10.1063/1.4940892.

Kanin, E., Garagash, I., Boronin, S. et al. 2024. Geomechanical Risk Assessment for CO_2 Storage in Deep Saline Aquifers. *J Rock Mech Geotech Eng*. https://doi.org/10.1016/j.jrmge.2024.04.016.

Kim, J., Tchelepi, H. A., and Juanes, R. 2013. Rigorous Coupling of Geomechanics and Multiphase Flow with Strong Capillarity. *SPE J.* **18** (6): 1123–1139. https://doi.org/10.2118/141268-PA.

Laesecke, A. and Muzny, C. D. 2017. Reference Correlation for the Viscosity of Carbon Dioxide. *J Phys Chem Ref Data* **46** (1). https://doi.org/10.1063/1.4977429.

Lewis, R. W. and Schrefler, B. A. 1998. *The Finite Element Method in the Static and Dynamic Deformation and Consolidation of Porous Media*. John Wiley & Sons. https://doi.org/10.1023/A:1004546808159.

Li, S., Li, X., and Zhang, D. 2016. A Fully Coupled Thermo-Hydro-Mechanical, Three-Dimensional Model for Hydraulic Stimulation Treatments. *J Nat Gas Eng* **34**: 64–84. https://doi.org/10.1016/j.jngse.2016.06.046.

Luu, K., Schoenball, M., Oldenburg, C. M. et al. 2022. Coupled Hydromechanical Modeling of Induced Seismicity From CO_2 Injection in the Illinois Basin. *JGR Solid Earth* **127** (5). https://doi.org/10.1029/2021JB023496.

March, R., Doster, F., and Geiger, S. 2018. Assessment of CO_2 Storage Potential in Naturally Fractured Reservoirs With Dual-Porosity Models. *Water Resour Res* **54** (3): 1650–1668. https://doi.org/10.1002/2017WR022159.

Meguerdijian, S. and Jha, B. 2021. Quantification of Fault Leakage Dynamics Based on Leakage Magnitude and Dip Angle. *Num Anal Meth Geomechanics* **45** (16): 2303–2320. https://doi.org/10.1002/nag.3267.

Meguerdijian, S., Pawar, R. J., Harp, D. R. et al. 2022. Thermal and Solubility Effects on Fault Leakage during Geologic Carbon Storage. *Int J Greenh Gas Control* **116**: 103633. https://doi.org/10.1016/j.ijggc.2022.103633.

Metz, B., Davidson, O., Coninck, H. C. et al. 2005. *IPCC Special Report on Carbon Dioxide Capture and Storage*. Cambridge University Press.

Mikelić, A. and Wheeler, M. F. 2013. Convergence of Iterative Coupling for Coupled Flow and Geomechanics. *Comput Geosci* **17** (3): 455–461. https://doi.org/10.1007/s10596-012-9318-y.

Miller, S. A., Collettini, C., Chiaraluce, L. et al. 2004. Aftershocks Driven by a High-Pressure CO_2 Source at Depth. *Nature* **427** (6976): 724–727. https://doi.org/10.1038/nature02251.

Nguyen, T. S., Guglielmi, Y., Graupner, B. et al. 2019. Mathematical Modelling of Fault Reactivation Induced by Water Injection. *Minerals* **9** (5): 282. https://doi.org/10.3390/min9050282.

Nield, D. A. and Bejan, A. 2017. *Convection in Porous Media*. Springer. https://doi.org/10.1007/978-3-319-49562-0.

Nordbotten, J. M., Celia, M. A., and Bachu, S. 2005. Injection and Storage of CO_2 in Deep Saline Aquifers: Analytical Solution for CO_2 Plume Evolution During Injection. *Transp Porous Med* **58** (3): 339–360. https://doi.org/10.1007/s11242-004-0670-9.

Pruess, K.. 2004. Numerical Simulation of CO_2 Leakage From a Geologic Disposal Reservoir, Including Transitions From Super- to Subcritical Conditions, and Boiling of Liquid CO_2. *SPE J*. **9** (02): 237–248. https://doi.org/10.2118/86098-PA.

Pruess, K. 2005. Numerical Studies of Fluid Leakage from a Geologic Disposal Reservoir for CO_2 Show Self-limiting Feedback between Fluid Flow and Heat Transfer. *Geophys Res Lett* **32** (14). https://doi.org/10.1029/2005GL023250.

Pruess, K. 2008. On CO_2 Fluid Flow and Heat Transfer Behavior in the Subsurface, Following Leakage from a Geologic Storage Reservoir. *Environ Geol* **54** (8): 1677–1686. https://doi.org/10.1007/s00254-007-0945-x.

Rinaldi, A. P., Vilarrasa, V., Rutqvist, J. et al. 2015. Fault Reactivation during CO_2 Sequestration: Effects of Well Orientation on Seismicity and Leakage . *Greenhouse Gases* **5** (5): 645–656. https://doi.org/10.1002/ghg.1511.

Ringrose, P., Atbi, M., Mason, D. et al. 2009. Plume Development around Well KB-502 at the In Salah CO_2 Storage Site. *First Break* **27** (1). https://doi.org/10.3997/1365-2397.27.1295.28744.

Rutqvist, J., Birkholzer, J., Cappa, F. et al. 2007. Estimating Maximum Sustainable Injection Pressure during Geological Sequestration of CO_2 Using Coupled Fluid Flow and Geomechanical Fault-Slip Analysis. *Energy Convers Manag* **48** (6): 1798–1807. https://doi.org/10.1016/j.enconman.2007.01.021.

Rutqvist, J., Graupner, B., Guglielmi, Y. et al. 2020. An International Model Comparison Study of Controlled Fault Activation Experiments in Argillaceous Claystone at the Mont Terri Laboratory. *Int J Rock Mech Min Sci* **136**: 104505. https://doi.org/10.1016/j.ijrmms.2020.104505.

Rutqvist, J., Rinaldi, A. P., Cappa, F. et al. 2016. Fault Activation and Induced Seismicity in Geological Carbon Storage – Lessons Learned from Recent Modeling Studies. *J Rock Mech Geotech Eng* **8** (6): 789–804. https://doi.org/10.1016/j.jrmge.2016.09.001.

Rutqvist, J., Wu, Y.-S., Tsang, C.-F. et al. 2002. A Modeling Approach for Analysis of Coupled Multiphase Fluid Flow, Heat Transfer, and Deformation in Fractured Porous Rock. *Int J Rock Mech Min Sci (1997)* **39** (4): 429–442. https://doi.org/10.1016/S1365-1609(02)00022-9.

Sáez-Leiva, F., Hurtado, D. E., Gerbault, M. et al. 2023. Fluid Flow Migration, Rock Stress and Deformation Due to a Crustal Fault Slip in a Geothermal System: A Poro-Elasto-Plastic Perspective. *Earth Planet Sci Lett* **604**: 117994. https://doi.org/10.1016/j.epsl.2023.117994.

Schrag, D. P. 2009. Storage of Carbon Dioxide in Offshore Sediments. *Science* **325** (5948): 1658–1659. https://doi.org/10.1126/science.1175750.

Settari, A. and Mounts, F. M. 1998. A Coupled Reservoir and Geomechanical Simulation System. *SPE J.* **3** (03): 219–226. https://doi.org/10.2118/50939-PA.

Shi, Y., Song, X., Li, J. et al. 2019. Numerical Investigation on Heat Extraction Performance of a Multilateral-Well Enhanced Geothermal System with a Discrete Fracture Network. *Fuel (Lond)* **244**: 207–226. https://doi.org/10.1016/j.fuel.2019.01.164.

Shipton, Z. K. and Cowie, P. A. 2003. A Conceptual Model for the Origin of Fault Damage Zone Structures in High-Porosity Sandstone. *J Struct Geol* **25** (3): 333–344. https://doi.org/10.1016/S0191-8141(02)00037-8.

Span, R. and Wagner, W. 1996. A New Equation of State for Carbon Dioxide Covering the Fluid Region from the Triple-Point Temperature to 1100 K at Pressures up to 800 MPa. *J Phys Chem Ref Data* **25** (6): 1509–1596. https://doi.org/10.1063/1.555991.

van Genuchten, M. Th. 1980. A Closed-form Equation for Predicting the Hydraulic Conductivity of Unsaturated Soils. *Soil Science Soc of Amer J* **44** (5): 892–898. https://doi.org/10.2136/sssaj1980.03615995004400050002x.

Vasco, D. W., Rucci, A., Ferretti, A. et al. 2010. Satellite-based Measurements of Surface Deformation Reveal Fluid Flow Associated with the Geological Storage of Carbon Dioxide. *Geophys Res Lett* **37** (3). https://doi.org/10.1029/2009GL041544.

Vilarrasa, V., Olivella, S., Carrera, J. et al. 2014. Long Term Impacts of Cold CO_2 Injection on the Caprock Integrity. *Int J Greenh Gas Control* **24**: 1–13. https://doi.org/10.1016/j.ijggc.2014.02.016.

White, C. M., Smith, D. H., Jones, K. L. et al. 2005. Sequestration of Carbon Dioxide in Coal with Enhanced Coalbed Methane Recovery—A Review. *Energy Fuels* **19** (3): 659–724. https://doi.org/10.1021/ef040047w.

Wu, Z., Cui, W., Weng, L. et al. 2023. Modeling Geothermal Heat Extraction-Induced Potential Fault Activation by Developing an FDEM-Based THM Coupling Scheme. *Rock Mech Rock Eng* **56** (5): 3279–3299. https://doi.org/10.1007/s00603-023-03218-1.

Yehya, A., Yang, Z., and Rice, J. R. 2018. Effect of Fault Architecture and Permeability Evolution on Response to Fluid Injection. *JGR Solid Earth* **123** (11): 9982–9997. https://doi.org/10.1029/2018JB016550.

Zappone, A., Rinaldi, A. P., Grab, M. et al. 2021. Fault Sealing and Caprock Integrity for CO_2 Storage: An in Situ Injection Experiment . *Solid Earth* **12** (2): 319–343. https://doi.org/10.5194/se-12-319-2021.

Zhao, X. and Jha, B. 2021. A New Coupled Multiphase Flow–Finite Strain Deformation–Fault Slip Framework for Induced Seismicity. *J Comput Phys* **433**. https://doi.org/10.1016/j.jcp.2021.110178.

Zhao, X. and Jha, B. 2022. Diagnostic and Predictive Analysis of Production and Injection-induced Fault Activation. *Num Anal Meth Geomechanics* **46** (2): 392–415. https://doi.org/10.1002/nag.3304.